2017

TUNING THE EFFECTIVE ELECTRON CORRELATION IN IRIDATE SYSTEMS FEATURING STRONG SPIN-ORBIT INTERACTION

John H. Gruenewald

University of Kentucky, john.gruenewald@uky.edu
Author ORCID Identifier:
 https://orcid.org/0000-0003-2133-0132
Digital Object Identifier: https://doi.org/10.13023/ETD.2017.514

STUDENT AGREEMENT:

I represent that my thesis or dissertation and abstract are my original work. Proper attribution has been given to all outside sources. I understand that I am solely responsible for obtaining any needed copyright permissions. I have obtained needed written permission statement(s) from the owner(s) of each third-party copyrighted matter to be included in my work, allowing electronic distribution (if such use is not permitted by the fair use doctrine) which will be submitted to UKnowledge as Additional File.

I hereby grant to The University of Kentucky and its agents the irrevocable, non-exclusive, and royalty-free license to archive and make accessible my work in whole or in part in all forms of media, now or hereafter known. I agree that the document mentioned above may be made available immediately for worldwide access unless an embargo applies.

I retain all other ownership rights to the copyright of my work. I also retain the right to use in future works (such as articles or books) all or part of my work. I understand that I am free to register the copyright to my work.

REVIEW, APPROVAL AND ACCEPTANCE

The document mentioned above has been reviewed and accepted by the student's advisor, on behalf of the advisory committee, and by the Director of Graduate Studies (DGS), on behalf of the program; we verify that this is the final, approved version of the student's thesis including all changes required by the advisory committee. The undersigned agree to abide by the statements above.

<div align="right">

John H. Gruenewald, Student

Dr. Ambrose Seo, Major Professor

Dr. Christopher Crawford, Director of Graduate Studies

</div>

TUNING THE EFFECTIVE ELECTRON CORRELATION IN IRIDATE SYSTEMS
FEATURING STRONG SPIN-ORBIT INTERACTION

DISSERTATION

A dissertation submitted in partial fulfillment of the
requirements for the degree of Doctor of Philosophy in the
College of Arts and Sciences
at the University of Kentucky

By
John Henry Gruenewald

Lexington, Kentucky

Director: Dr. Ambrose Seo, Professor of Physics

Lexington, Kentucky

2017

ABSTRACT OF DISSERTATION

TUNING THE EFFECTIVE ELECTRON CORRELATION IN IRIDATE SYSTEMS
FEATURING STRONG SPIN-ORBIT INTERACTION

The $5d$ transition metal oxides have drawn substantial interest for predictions of being suitable candidates for hosting exotic electronic and magnetic states, including unconventional superconductors, magnetic skyrmions, topological insulators, and Weyl semimetals. In addition to the electron-electron correlation notable in high-temperature $3d$ transition metal superconductors, the $5d$ oxides contain a large spin-orbit interaction term in their ground state, which is largely responsible for the intricate phase diagram of these materials. Iridates, or compounds containing $5d$ iridium bonded with oxygen, are of particular interest for their spin-orbit split $J_{eff} = 1/2$ state, which is partially filled without the presence of any additional electron correlation. However, the comparable energetics between a small, finite electron correlation energy and the spin-orbit interaction make the band structure of iridates amenable to small perturbations of the crystalline lattice and ideal for exploring the interplay between these two interactions.

While altering the spin-orbit interaction strength of iridium is tenably not feasible, the electron correlation energy can be tuned using a variety of experimental techniques. In this dissertation, the electronic and magnetic properties of iridates at various electron correlation energies are studied by altering the epitaxial lattice strain, dimensionality, and the radius size of the A-site cation. These parameters tune the effective electronic bandwidth of the system, which is inversely proportional to the effective electron correlation energy. The lattice strain and the cationic radius size achieve this by altering the Ir-O-Ir bond angle between nearest neighbor Ir ions. In the case of dimensionality tuning, the effective bandwidth is controlled via the coordination number of each Ir ion.

In the first study, a metal-to-insulator transition is observed in thin films of the semi-metallic $SrIrO_3$ as in-plane compressive lattice strain is increased. This observation is consistent with the expectation of compressive lattice strain increasing the effective correlation energy; however, optical spectroscopy spectra reveal the increase is not sufficient for opening an insulating Mott gap. In the second part, the effective correlation energy is adjusted using a dimensional confinement of the layered iridate Sr_2IrO_4. Here, the coordination number of each Ir ion is reduced using an a-axis oriented superlattice of one-dimensional IrO_2 quantum stripes, where several emergent features are revealed in its

insulating $J_{\text{eff}} = 1/2$ state. In the final study, the effective correlation is tuned in a series of mixed-phase pyrochlore iridate thin films, where the Ir atoms take a corner-shared tetrahedral configuration. Here, a transition between conducting to insulating magnetic domain walls is revealed as the correlation energy is increased via A-site chemical doping. Each of these studies sheds light on the pronounced role the effective correlation energy plays in determining the local subset of phases predicted for iridates and related systems featuring strong spin-orbit interactions.

KEYWORDS: iridates, electron correlation, spin-orbit interaction, low dimensional materials, thin film oxides

John H. Gruenewald
Author of Dissertation

December 5, 2017
Date

TUNING THE EFFECTIVE ELECTRON CORRELATION IN IRIDATE SYSTEMS
FEATURING STRONG SPIN-ORBIT INTERACTION

By

John Henry Gruenewald

Dr. Ambrose Seo
Director of Dissertation

Dr. Christopher Crawford
Director of Graduate Studies

December 5, 2017
Date

This work is dedicated to my father, Richard, for giving me my first physics book and teaching me to rest if I must, but never quit;

to my mother, Joyce, for being a true inspiration and instilling courage and hope in all the times I needed it the most;

and to my brother, David, for being my role model and reminding me that there's some good in the world… and it's worth fighting for.

ACKNOWLEDGEMENTS

TABLE OF CONTENTS

LIST OF TABLES

LIST OF FIGURES

Chapter 1   Introduction

1.1   Background

In 1908, Heike Kamerlingh Onnes successfully liquified helium and thus was able to experimentally probe materials at temperatures as low as 1.5 K. This experimental accomplishment allowed for the highly anticipated exploration of material properties at low temperature, which had been merely speculative before that point. In just three years after his initial discovery, Onnes discovered an entirely new phenomenon at low temperature where the electrical resistance of mercury abruptly vanished around 4.2 K – a phase transition today known as superconductivity (5). This sparked a revolution both experimentally and theoretically in the physics community; however, the progress forward remained daunting. While many phenomenological models had been developed, it would be another 46 years from its initial discovery before a coherent microscopic theory of superconductivity is developed by Bardeen, Cooper, and Schrieffer known as BCS theory (6). Experimentally, the task of finding materials with a higher superconducting transition temperature T_c seemed an exercise in futility, and before 1986 the highest recorded T_c was that of Nb_3Ge at 23 K (7). Although this was far from room temperature, the observations were consistent with BCS theory, namely that the superconducting gap energy E_g is relatively small for metals ($E_g \sim 10^{-4}$ eV (8)) and weak thermal excitations are sufficient for quenching the superconducting state.

After 75 years from the initial discovery, Georg Bednorz and Karl Müller made another breakthrough in the field when they measured a superconducting transition at 35 K in the room temperature, semiconducting oxide system of $(Ba_\delta La_{5-\delta})Cu_5O_{5(3-x)}$, an increase of over 50% from the previous record (9). Just one year later, Maw-Kuen Wu and

Chu Ching-wu measured a T_c of 93 K in the oxide of $Y_{1+\delta}Ba_{1-\delta}CuO_4$ (10), which was the first material observed to superconduct above liquid nitrogen temperatures. Unlike the previous class of superconducting metallic alloys, these high-T_c oxides take a *K_2NiF_4*-type structure, i.e. effectively two-dimensional systems consisting of layered two-dimensional planes of CuO_2 planes each separated by electronically inert rock salt layers. The reduced dimensionality in this system allows for additional crystalline interactions to become relevant in the ground state Hamiltonian, such as the 'on-site' Coulomb repulsion or electron-electron interaction, which will be discussed in further detail throughout this thesis. While the exact microscopic mechanism for the superconductivity in these systems is still contested, the new epoch in condensed matter physics following the observations in these materials with a large electron correlation energy goes undisputed. In 1987, Georg Bednorz and Karl Müller were awarded the Nobel prize in physics, which was less than two years after their initial discovery (11).

The work in this thesis focuses on tuning the electron correlation in thin-films of a related oxide system known as the iridates, which consist of compounds featuring the *5d* transition metal iridium coordinated by an octahedral oxygen environment. This system features not only the Hubbard interaction relevant in the high-T_c cuprate materials, but also an additional spin-orbit interaction due to the large atomic number Z of iridium ($H_{SO} \propto Z^4$). The introduction chapters (Chapter 1 and Chapter 2) will describe the context of how these interactions emerge in iridate systems, and the experimental synthesis technique of pulsed laser deposition used in developing these crystals. In the first study described in Chapter 3, the meta-stable phase of three-dimensional $SrIrO_3$ is epitaxially stabilized on substrates of various lattice mismatch, and the effects of this bandwidth engineering are

clear in a metal-insulator transition observed in this compound's electronic transport properties. In the next study (Chapter 4), the two-dimensional analogue of $SrIrO_3$, i. e. the layered Sr_2IrO_4 compound, is synthesized as a dimensionally confined superlattice material in the *a*-axis orientation. From our structural and electronic characterizations, this superlattice approach effectively tunes this two-dimensional material into a superlattice of one-dimensionally confined stripes. This study sets the ground work for a generalizable methodology for creating one-dimensional materials from two-dimensional layered materials. And finally, in Chapter 5, a tuning of the effective correlation energy is performed on a series of mixed phase pyrochlore iridates, where the Ir-O network form corner-sharing tetrahedra of frustrated spin-configurations. While these films have more defects than bulk single crystals, the magneto-conductance in these mixed-phase films is consistent with the expected spin-flip transitions for tuning U_{eff} and offers supporting evidence for the robust nature of several distinct topological states in these systems.

Taken together, the studies of this dissertation illustrate the wide-range of electronic and magnetic properties accessible in iridates, where the multiple interactions are highly tunable by the underlying dimension and lattice structure. While highly tunable systems are often times difficult for achieving a certain level of experimental dependency, they offer ample opportunity for studying a large variation of interesting phenomena and phases– and under the right experimental conditions, just might open the door for discovering the next pivotal breakthrough.

1.2 Origin of the spin-orbit interaction

For most atoms, the spin-orbit interaction is a small correction to the ground state Hamiltonian and, in the solid state, is usually dominated by other competing energies in a

crystalline lattice, such as the Coulomb interaction and crystal field splitting. The spin-orbit interaction is a relativistic effect that arises from the coupling between an electron's magnetic moment due to spin $\boldsymbol{\mu_e}$ and the magnetic field $\boldsymbol{B}$ an electron experiences while orbiting an atomic nucleus of charge Ze, where Z is the atomic number of the nucleus and e is the elementary charge. From the rest frame of the electron, the magnetic field generated by the orbiting nucleus on the electron at distance $\boldsymbol{r}$ is given by the Biot-Savart law:

$$\boldsymbol{B} = -\frac{Ze}{c}\frac{\boldsymbol{v} \times \boldsymbol{r}}{r^3}, \tag{1.1}$$

where $-\boldsymbol{v}$ is the velocity of the moving atomic nucleus. Thus, the classical spin-orbit energy between the electron's dipole moment and $\boldsymbol{B}$ is:

$$H_{SO} = -\boldsymbol{\mu}_e \cdot \boldsymbol{B}$$

$$= \frac{Ze}{mc}\frac{\boldsymbol{\mu}_e \cdot (\boldsymbol{p} \times \boldsymbol{r})}{r^3}$$

$$= -\frac{Ze}{mc}\frac{\boldsymbol{\mu}_e \cdot \boldsymbol{l}}{r^3}. \tag{1.2}$$

Now substituting the magnetic moment of the electron ($\boldsymbol{\mu_e} = -(e/mc)\boldsymbol{S}$) and the quantized angular momentum $\boldsymbol{L}$ for $\boldsymbol{l}$, the spin-orbit Hamiltonian becomes:

$$H_{SO} = \frac{Ze^2}{2(mc)^2}\frac{\boldsymbol{S} \cdot \boldsymbol{L}}{r^3}, \tag{1.3}$$

where a factor of 1/2, known as the Thomas factor, must be included in order to account for the noninitial rest frame of the electron as it orbits the nucleus (12). To find the energy eigenvalues of this Hamiltonian, it must be rewritten in a basis that diagonalizes the Hamiltonian, i. e. $\boldsymbol{S} \cdot \boldsymbol{L}$ must be rewritten to commute with H_{SO}. Considering the total angular momentum $\boldsymbol{J} = \boldsymbol{L} + \boldsymbol{S}$, the Hamiltonian can be written as:

$$H_{SO} = \frac{Ze^2}{4(mc)^2} \frac{1}{r^3} [J^2 - L^2 - S^2]. \qquad (1.4)$$

Diagonalizing this Hamiltonian in this basis yields:

$$\langle H_{SO} \rangle = E_{SO}$$

$$= \frac{Ze^2}{4(mc)^2} \langle \frac{1}{r^3} \rangle \hbar^2 \left[j(j+1) - l(l+1) - \frac{3}{4} \right], \qquad (1.5)$$

where $s = 1/2$ for spin-1/2 electrons. Evaluating the expectation value of $1/r^3$ with n degenerate ground states yields:

$$\langle \frac{1}{r^3} \rangle = \frac{Z^3}{a_0^3} \frac{1}{n^3 l(l+1/2)(l+1)}, \qquad (1.6)$$

where a_0 is the Bohr atomic radius (13). Now substituting this result into Equation (1.5), the spin-orbit interaction energy becomes:

$$E_{SO} = \frac{Z^4 e^2 \hbar^2}{4(mc)^2 a_0^3} \frac{\left[j(j+1) - l(l+1) - \frac{3}{4} \right]}{n^3 l(l+1/2)(l+1)}. \qquad (1.7)$$

From the leading factor, this calculation indicates that the spin-orbit energy becomes a significant interaction for atoms with large atomic numbers, i. e. $E_{SO} \propto Z^4$. Hence, this effect is much more pronounced in compounds containing *5d* transition metals, such as in the iridates, than in the smaller atomic numbers found in the *3d* transition metals, such as in the cuprates. It is also important to note that while other crystalline energies can be more accessibly tuned experimentally, the spin-orbit interaction is a fixed quantity dictated by the atoms. While this interaction plays an important role in shaping the physics of iridate systems, it must also compete energetically with another important interaction known as the effective electron correlation energy.

1.3   The effective electron correlation energy

For noninteracting band metals and insulators, the periodic potential of the crystalline lattice dictates the energy bands, and a material is considered a metal (insulator) if the highest occupied band is partially (fully) filled. This Bloch band picture had been very successful in describing the electronic properties of many materials, but failed to describe the insulating behaviors observed in certain partially filled *3d* transition metal oxide systems (14). For these class of materials, the electron-electron correlation energy is more relevant in determining the electronic structure.

The electron-electron correlation energy is the result of the Coulomb repulsion between electrons occupying the same atomic site on a crystalline lattice. By Coulomb's law, the electrostatic repulsion energy between two electrons occupying a single site is $\sim \frac{e^2}{r}$, with *r* being on the order of an angstrom. This implies that strongly interacting systems have an energy cost on the order of several eV for multiple electron occupancy on a single site. If this energy cost is larger than the Fermi energy, then a strongly interacting material with a partially filled valence band will fail to conduct. These types of materials are known as Mott insulators and are largely responsible for the interesting phenomena observed in *3d* transition metal oxides, such as high-T_c superconductivity and colossal magnetoresistance (1).

The Hubbard model is a single-band Hamiltonian model which approximates the on-site Coulomb repulsion on crystalline lattices. This model includes an electron-electron interaction term H_U in the Hamiltonian and is written in a second quantization form as:

$$H_U = U \sum_i n_{i\uparrow} n_{i\downarrow}, \qquad (1.8)$$

where $n_{i\uparrow}$ ($n_{i\downarrow}$) is the number of electrons with spin up (down) on atomic site i, and $U > 0$ is the repulsive interaction energy (15). The Hubbard U gives an energetic cost to the ground state Hamiltonian for two electrons occupying the same site. The total Hamiltonian of the interacting system includes two additional terms:

$$H = H_t + H_U - \mu N, \qquad (1.9)$$

where H_t is the kinetic hoping term borrowed from the tight binding approximation and μN is the electron fill factor. In the second quantization form, H_t can be written as:

$$H_t = -t \sum_{\langle ij \rangle} \left(c_{i\sigma}^\dagger c_{j\sigma} + H.c. \right), \qquad (1.10)$$

where the operator $c_{j\sigma}$ annihilates an electron at atomic site i and the operator $c_{i\sigma}^\dagger$ creates an electron at nearest neighboring site j. When acted on an atomic lattice, this term acts to move electrons between neighboring atomic sites with hopping amplitude t, which is proportional to the bandwidth of the system. It is important to note the difference in sign between H_t and H_U. The kinetic term H_t lowers the system's energy by allowing electron hopping across neighboring sites, while the Hubbard interaction acts to localize single electrons on each atomic site and hence prevent hopping. The dominating term will determine the electronic properties of the interacting system. Due to the competing nature between these parameters, it is convenient to define an effective electron correlation energy $U_{\text{eff}} \equiv \frac{U}{t}$. This U_{eff} can be tuned via the bandwidth of the system (proportional to t) and at a critical value, drive a half-filled metallic ground state into a gapped insulating state (see Figure 1.1). The tuning of U_{eff} in this manner is important, as the bandwidth of a crystalline

lattice can be controlled using a variety of experimental techniques. In the work pertaining

to this thesis, the bandwidth is controlled using applications of lattice strain, crystalline

dimensionality, and dopant size.
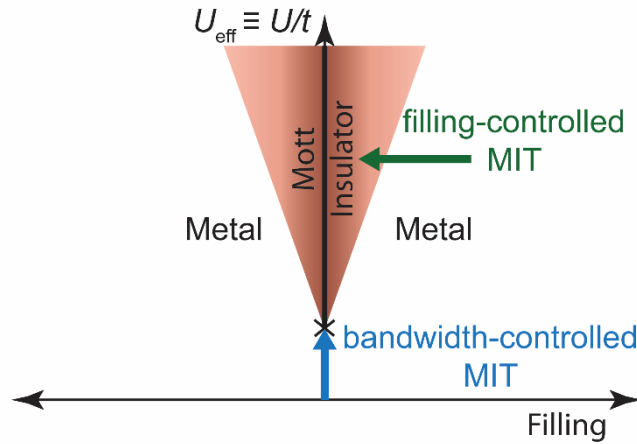
Figure 1.1: Possible metal-insulator transitions from the Hubbard model. Along the vertical axis, the U_{eff} increases and at a critical point, opens a gap in the metallic ground state. Traversing the horizontal axis from right to left, the filling factor is reduced, and a metal-insulator transition occurs at a particular point within the shaded region. The region closest to the vertical takes a Mott insulating ground state. This figure has been adopted from Ref. (1).

Chapter 2   Experimental methods

Pulsed laser deposition (PLD) is a widely used method for growth of various thin-films, superlattices, and heterostructures (16,17). It has been used extensively over the past two decades in the development of thin-films which exhibit interesting physical properties such as strongly-correlated electronic materials (18), high-temperature superconductors (19), colossal magnetoresistance materials (17), ferroelectrics (20), compound semiconductors, and nanocrystalline materials (21).

PLD has remained popular for several reasons: it features the stoichiometric transfer of the target material to the film; it is compatible with both low and high vacuum pressure environments ($\leq$ 0.5 Torr); and multiple materials can be easily added to a system for heterostructure synthesis. Additionally, atomic-scale oxide thin-films and heterostructures grown by PLD are shown to be comparable to samples grown by molecular beam epitaxy (MBE) (22,23).   Reflection high-energy electron diffraction (RHEED) has been successfully used to monitor the film growth in real-time by measuring the structural reconstruction and number of unit-cell layers (24-27). However, the requirement of low-pressure operation and its inability to assess a material's electronic structure are a few shortcomings of RHEED. While advanced multiple-stage RHEED has overcome the first problem by increasing the maximum operational oxygen partial pressure to 0.5 Torr (28,29), there remains a huge demand for *in situ* monitoring of the electronic structure of a material during growth. Optical spectroscopic ellipsometry (SE), which is operational regardless of partial pressure, has been used as an alternative method to monitor a sample's electronic structure in real-time (29-31). However, SE is not used as frequently as RHEED since a complicated modeling process is required to analyze the SE data. Moreover, when

9

in situ SE is performed without any additional supporting measurements, the results of the modeling process are difficult to validate due to multiple unknowns, e. g. fit parameters such as thin-film thickness and complex optical constants.

2.1 Pulsed Laser Deposition System Overview

Our PLD system with dual *in situ* SE and RHEED components is schematically drawn in Figure 2.1. The vacuum chamber is custom-made (Rocky Mountain Vacuum Tech.) in order to optimize data acquisition and to enable simultaneous real-time *in situ* measurement of RHEED and Spectroscopic Ellipsometry (SE). There are six ports specifically designed and implemented into this system to perform dual *in situ* RHEED and SE measurements. Two of these ports are used by the RHEED electron gun and detector (Phosphor screen and CCD camera assembly). They are positioned such that the electron beam is incident at a grazing angle to a substrate (sample) surface inside the chamber. The other four ports are positioned such that *in situ* ellipsometry can be performed simultaneously with RHEED at the angles of either 65° (not pictured in Figure 2.1) or 75° to the substrate's surface normal direction. There is also an additional antireflection-coated quartz viewport for the pulsed excimer laser and is positioned such that focused laser beam pulses are incident to the target at an angle of 45°. While conventional PLD systems have been designed to perform either *in situ* RHEED or SE, our system is optimized for the simultaneous monitoring of both RHEED and SE, which better equips us to interpret the *in situ* data as discussed below.

The RHEED consists of an electron gun (Staib 30 kV model), a phosphor screen, and a charge-coupled device (CCD) camera (shielded from external light by a screen) attached to the PLD chamber. The electron beam is incident to the surface of the substrate

at a grazing angle ($\leq 3°$) and the reflected electron beam is collected by the phosphor screen

and is measured by the CCD camera.
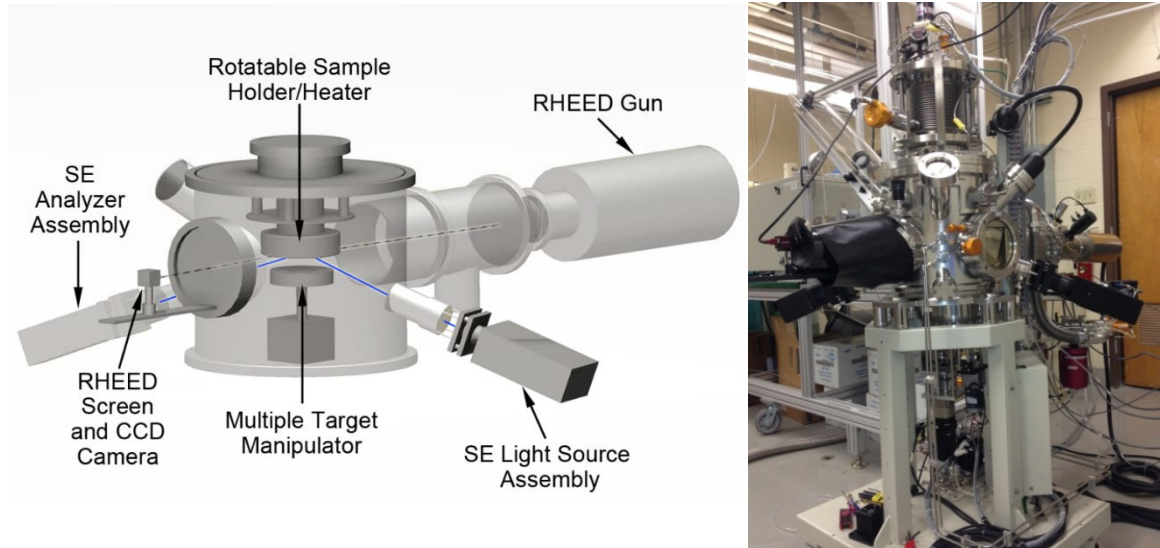
Figure 2.1: Schematic drawing (left) and photograph (right) of the PLD system with dual *in situ* RHEED and spectroscopic ellipsometry components taking simultaneous measurements. The RHEED gun, multiple target manipulator, and heater are contained within the vacuum chamber while the CCD camera, SE source, and analyzer assemblies are secured to external ports.

The SE (J. A. Woollam M-2000-210 *in situ* model) consists of light source and

analyzer assemblies mounted to the PLD chamber. White light from a broadband Xenon

arc lamp is polarized in the SE source assembly by a linear polarizer and compensator. The

light beam reflects off the sample and is directed to a rotating analyzer in the SE analyzer

assembly, which is sent to a spectrometer (monochrometer)/CCD detector through an

optical fiber. In our system, the SE source and analyzer assemblies can be mounted to the

PLD chamber with an incident angle of either 65° or 75° relative to the sample's normal

axis, which are close to the Brewster angles and are good for characterizing many oxide

thin-films (32,33). The SE can take real-time dynamic scans every 25 ms in the spectral

range of 210 – 1000 nm in wavelength (1.2 – 5.9 eV in photon energy). The spectral range

of the SE is chosen for oxide materials, which allows for the monitoring of optical

transitions between the correlated electron bands (Hubbard bands) and the charge-transfer transitions between the O $2p$ band and transition-metal d bands.

In order to enable the simultaneous monitoring, the substrate holder (heater) is made rotatable with an adjustable (both tilting and height) z-axis stage so that the initial specular reflection of both RHEED and SE can be maximized. During the growth of a thin-film, the RHEED and SE data are simultaneously and continuously taken (maximum data acquisition rate of up to 40 Hz) without the need of suspending growth. The chamber is designed to enable sample alignment with the electron and photon beams by adjusting both the height and azimuthal angle of the sample holder. This is essential to perform both RHEED and SE measurements simultaneously during the entire growth process (Figure 2.1).

2.2   Reflection high-energy electron diffraction (RHEED)

Figure 2.2a-c and d show the RHEED diffraction patterns and intensity oscillations, respectively, taken during the growth of an $LaMnO_{3+\delta}$ (LMO) thin-film on a single crystalline $SrTiO_3$ (STO) substrate oriented such that (001) is out-of-plane. At the initiation of the deposition process, the electron beam is incident at a grazing angle to an atomically flat STO substrate prepared using the method described in Ref. (34). The oscillations of the intensity curve in Figure 2.2d show that LMO unit-cell layers are being deposited on the STO substrate, but the monotonic decay of the intensity curve indicates island growth is also occurring (layer-by-layer + island growth mode) (26,35). In addition, this decay of the intensity is typically seen when there is a lattice mismatch between the thin-film and the substrate (36). However, the time scale of the decay is much larger than that of the oscillations, so a reasonably smooth epitaxial growth of the LMO thin-film can be deduced
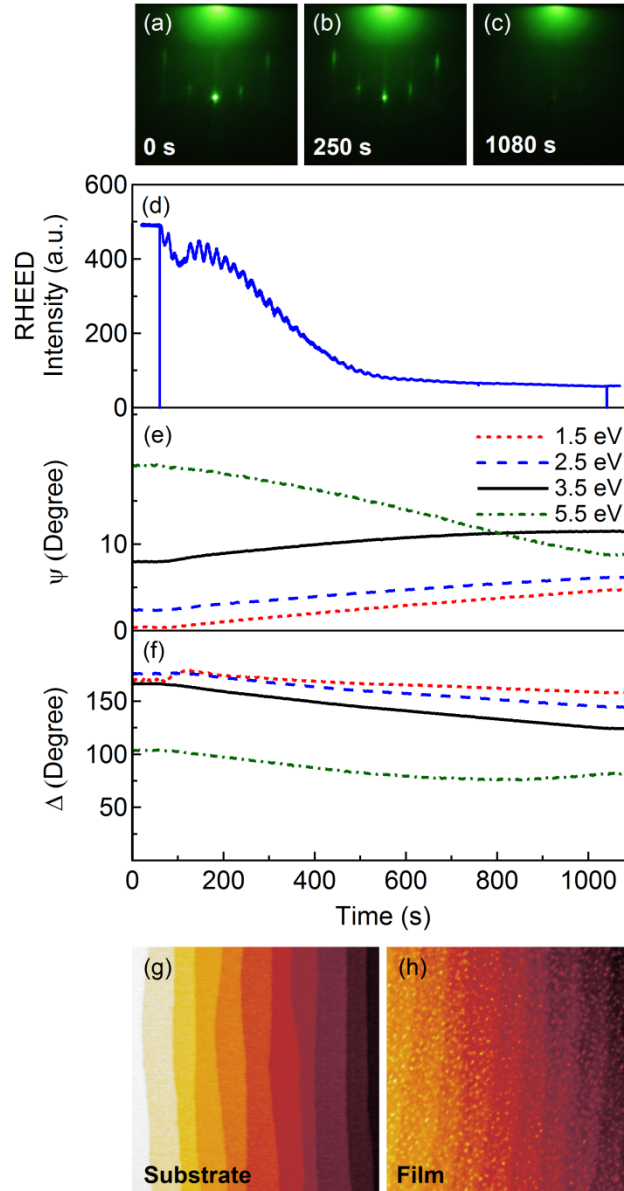
Figure 2.2: *In situ* data taken simultaneously by RHEED and SE during the growth of a LMO thin-film on an STO substrate. RHEED diffraction patterns taken at times (a) 0 s, (b) 250 s, and (c) 1080 s. (d) The RHEED intensity oscillations of one of the diffraction peaks during the growth. The two vertical lines indicate the start and finish of growth. Using the RHEED oscillations and the assumption of 1 oscillation/unit cell, the LMO can be reasonably estimated as being 6 nm thick during the first 400 s of growth. The SE dynamical spectra taken of (e) Ψ and (f) Δ at 0.5 Hz indicate the presence of the additional LMO band structure during its film growth at constant energy slices. Surface topology of (g) STO substrate and (h) LMO thin-film taken *ex situ* by AFM indicate the growth was a combination of the layer-by-layer and island growth mode. The growth conditions used during the deposition are an oxygen partial pressure P_{O2} of 30 mTorr with a substrate temperature T_s of 700°C.

from the RHEED intensity pattern. Additional *ex situ* measurements, such as atomic force

microscopy (AFM) are also important in final thin-film characterization and aids in validating the measurements made by the *in situ* SE and RHEED. According to the *ex situ* AFM topographic images of the sample before and after the growth, the thin-film still retains the step terraces of the substrate (see Figure 2.2g and h). Hence, the thin-film's surface roughness is on the atomic scale and can be neglected in SE modeling even though the growth is not a perfect layer-by-layer growth. The RHEED patterns and intensity oscillations can be used to monitor the film's surface reconstruction and the number of unit-cell layers, respectively. These RHEED measurements of the thin-film deposition give indispensable information to validate the model used in extracting the optical constants from the SE spectra, as described in Section 2.3 below. In our test growth, we observed clear RHEED intensity oscillations during the first 400 s of the deposition, corresponding to the LMO thin-film having a thickness of roughly 6 nm (15 unit-cells of LMO).

2.3   Optical spectroscopic ellipsometry

Polarized light from the *in situ* SE is incident upon the sample, and the two polarization states parallel (p) and perpendicular (s) to the plane of incidence are each changed separately according to the complex Fresnel reflection and transmission coefficients $\tilde{R}_i$ and $\tilde{T}_i$, where $i = p, s$ for p-polarized and s-polarized light, respectively (37). These coefficients directly determine each reflected polarization's attenuation $|R_i|$ and phase change δ_i. The light beam is then sent through the SE's rotating analyzer and the resulting intensity modulation is measured by a CCD array detector. The modulated signal can be fit to a Fourier series whose first two coefficients are determined by the Hadamard method. These coefficients, along with the initial p- and s- polarization state

14

intensities, are used to find the relative attenuation $|\tilde{R}_p|/|\tilde{R}_s|$ and phase change shift $\delta_p -$

δ_s of the reflected light beam. In ellipsometry, it is convenient to define

$$\tan \Psi \equiv \frac{|\tilde{R}_p|}{|\tilde{R}_s|} \tag{2.1}$$

$$\Delta \equiv \delta_p - \delta_s \tag{2.2}$$

$$\rho \equiv \tilde{R}_p/\tilde{R}_s = \tan \Psi \, e^{i\Delta}. \tag{2.3}$$

The angles Ψ and Δ are the ellipsometer angles measured by the SE and represent the

differential changes in amplitude and phase experienced upon reflection by the two *p*- and
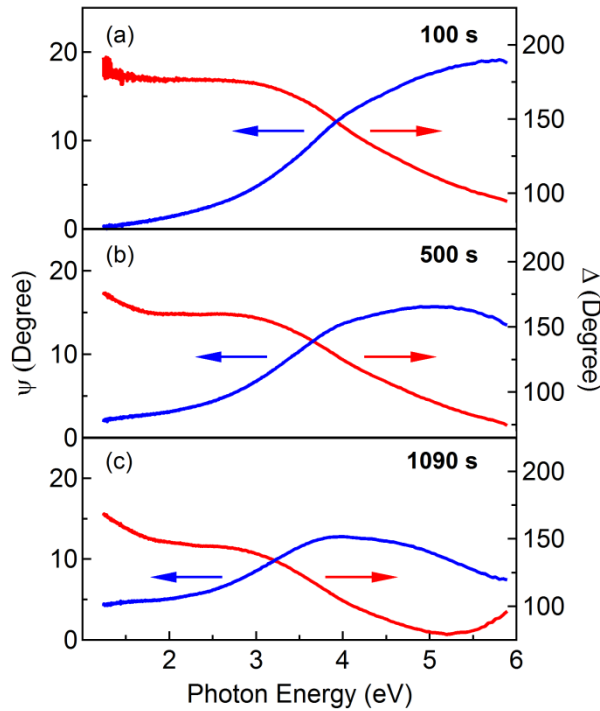
Figure 2.3: Full SE spectral scans taken from 1.2 eV to 5.9 eV are shown at times (a) 0 s , (b) 500 s, and (c) 1090 s during the LMO film deposition. By applying the appropriate model, the real-time optical constants, dielectric functions, and thickness evolution can be extracted from these spectra.

s- polarization components. The $\tan \Psi$ and $\cos \Delta$ are measured for the full spectral range

of the light source (1.2 – 5.9 eV). During the growth of a thin-film on a substrate, the *in*

situ SE can take dynamic full spectra at 40 Hz. Figure 2.2e and f show the real-time evolution of Ψ and Δ at four arbitrary photon energies as measured by our *in situ* SE for the same LMO thin-film grown on an STO substrate as discussed above. Figure 2.3 shows full SE spectral scans of this growth at times 0 s, 500 s, and 1090 s. Since our test growth of an LMO thin-film on an STO substrate is slow, we are able to achieve reasonably good data by choosing an acquisition rate of 0.5 Hz. Using these measured values of Ψ and Δ, the real-time optical constants, dielectric functions, and the LMO film thickness can be obtained through a modeling process described below.

The growth rate of the thin-film can be independently monitored by both the RHEED and SE (see Figure 2.4c), acting as an experimental control for consistency between the two measurement devices. To find real-time film thickness and optical constants of the sample from the SE, the ellipsometry angles Ψ and Δ are used as input parameters to an appropriate sample model. The biggest advantage of simultaneous monitoring lies in the ability to use RHEED's diffraction and intensity patterns to choose and validate appropriate models which can be used in analyzing the *in situ* SE spectra. The comprehensive model analysis required to interpret SE data has been a formidable task to accomplish in real-time measurements since it is rather difficult to obtain both thickness and optical parameters of thin-films using only SE data. Since we can obtain the information of a thin-film's growth mode and thickness by RHEED, we can bring more credibility to the SE spectral modeling process used for extracting the optical parameters from the SE spectra.

From Section 2.2   Reflection high-energy electron diffraction (RHEED), the RHEED intensity curve (Figure 2.2d) and RHEED diffraction patterns (Figure 2.2a-c)

indicate a 'layer-by-layer + island' growth of LMO on the STO substrate with surface

roughness on the atomic scale. We confirmed these results with *ex situ* AFM as illustrated

in Figure 2.2h. These measurements reasonably justify modeling this sample as a thin,

isotropic smooth layer (layer 1) on an isotropic substrate (layer 2) in an isotropic ambient

(layer 0). When an appropriate model is applied, the optical constants and film thickness

can be found from SE spectra. The complex Fresnel reflection coefficients for this three-

phase system are found and are related to the SE spectra (Ψ and Δ) by Eq. (2.3) (see

Appendix Fresnel reflection coefficients for isotropic single slab model for calculation

details). From this relation, the thin-film's complex index of refraction N_1 ($N = n + ik$)

and thickness can be numerically calculated at any time during the growth using proper

initial values at each photon energy. Figure 2.4a and Figure 2.4b show the distinguishable

n and *k* spectra for the LMO thin-film and substrate both extracted at the end of the growth

period.

Figure 2.4c shows the real-time thickness of the LMO thin-film monitored by both

SE and RHEED. From the RHEED intensity oscillations, the number of deposited LMO

crystal layers is measured and the thickness is calculated by assuming each LMO unit cell

has a thickness of ~3.95 Å (38). Note that we used this thickness information acquired

from RHEED to obtain the initial input parameters in our SE modeling process. The SE

and RHEED thickness curves each yield consistent linear deposition rates of ~ 0.238 Å/s

and ~ 0.208 Å/s, respectively. Therefore, SE and RHEED collectively enable the overall

film thickness to be determined in real-time during the entire growth process. Although

the RHEED oscillations disappear after c.a. 400 s of growth, the same SE model is applied

during the entire deposition. Both the SE and RHEED result in consistent thickness in the

initial growth of the LMO thin-film, and SE can be used for thickness monitoring when the RHEED oscillations disappear, offering another advantage of simultaneous *in situ* monitoring. For example, if the LMO thin-film grown on STO described above was
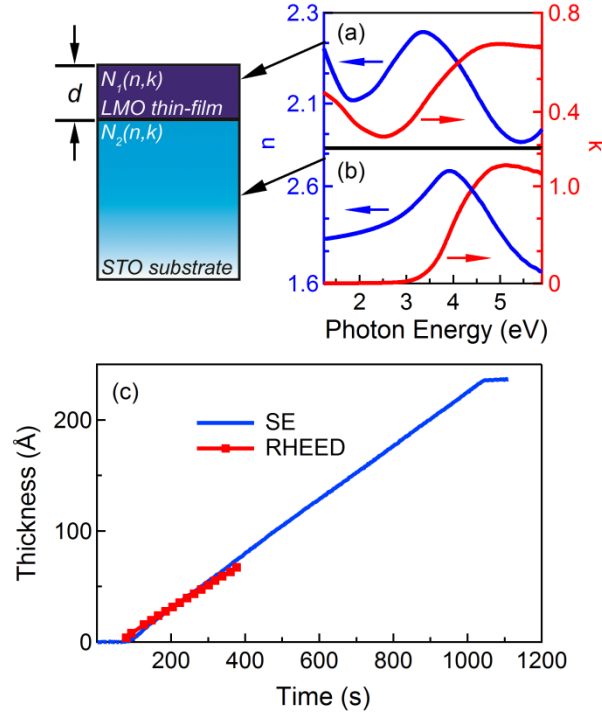
Figure 2.4: An isotropic single slab model is applied to the SE spectra to obtain the thin film's real-time optical constants and thickness information. The optical constants from 1.2 – 5.9 eV for the (a) LMO thin-film $N_1(n,k)$ and (b) STO substrate $N_2(n,k)$ obtained from the *in situ* SE spectra at the end of the growth period. (c) Real-time thickness of LMO thin-film during the growth as determined independently by RHEED and SE. The measurements are self-consistent and support the validity of the model used to extract the optical constants and thickness from the SE spectra.

deposited in a chamber with only SE, there would be no knowledge of the film's *real-time* thickness during growth. Note that various *ex situ* characterizations are still very important but cannot provide *real-time* information during growth.

To obtain the electronic properties of the thin-film, the optical constants n and k can be converted into the complex dielectric function $\tilde{\varepsilon}(\varepsilon_1, \varepsilon_2)$ using the following relations:

$$\varepsilon_1 = n^2 - k^2 \tag{2.4}$$

$$\varepsilon_2 = 2nk, \tag{2.5}$$

where ε_1 and ε_2 are the dispersion (real) and absorption (imaginary) components of the thin-film's complex dielectric function, respectively. The real-time dielectric functions can show the time evolution of bandgap energies and optical transitions during the entire deposition process. Figure 2.5 displays the complex dielectric function of the film at 100 s, 300 s, and 1090 s during the growth. The dispersion ε_1 and absorption ε_2 depend strongly on the thickness of the LMO thin-film. The *d-d* transitions at about 1.5 eV are initially suppressed during the growth. An appreciable spectral weight transfer in this narrow energy range of 1 eV – 6 eV is also apparent from Figure 2.5. At this moment, it is not clear what physical mechanism governs the thickness dependent spectral weight transfer, which is left for future study. The important point is that the simultaneous use of RHEED
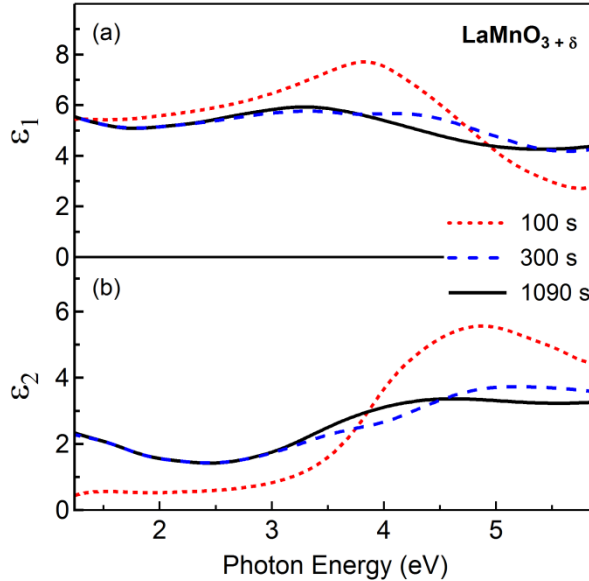
Figure 2.5: Real-time dielectric function of thin-film at various times during growth. The (a) dispersion ε_1 and (b) absorption ε_2 coefficients as obtained by applying Equations (2.4) and (2.5) to the SE optical constants extracted at 100 s, 300 s, and 1090 s.

and SE enable us to model and extract the real-time dielectric functions of thin-films by reducing the number of unknown variables using the thickness information obtained from RHEED.

Note that the high temperature optical properties measured at the growth temperature (~ 700 °C) are closely related to the thin-films' low temperature electronic properties and give us important information about their electronic structure (39). For example, although band gap energies usually decrease with increasing temperature, they are material specific and are altered much more significantly by factors such as dopants or electronic structural change than by thermal effects. Note that, Kamaras et $al.$ (40) demonstrated that depleting the oxygen content in $YBaCuO_{7-\delta}$ thin-films will change the films from a superconducting to a non-superconducting state; however, little temperature dependence was found in the optical spectra of these thin-films. Since in $situ$ optical spectra are also sensitive to doping or thin-film thicknesses, we might be able to monitor important parameters such as oxygen deficiencies in oxide thin-films (30). If there is a change in the dielectric functions (and bandgap energies) during growth, we need a rather sophisticated model to extract the optical parameters quantitatively. However, it is still possible to monitor the change qualitatively using a simple model. For example, in our growth of LMO, changes in the thickness dependence of the complex dielectric functions are observed even by using a simple thin, isotropic smooth layer-model (see Figure 2.5).

Our simultaneous real-time RHEED and SE technique can be effectively used for growing thin-films with targeted properties. For instance, tuning electronic properties such as band-gap energies can be done during the growth by directly monitoring the sample's optical spectra SE and adjusting the growth parameters during deposition. If a solid

understanding of the relationship between the dielectric functions and the surface reconstruction of a thin-film layer is established, then the RHEED diffraction patterns will provide insight to choose a proper model for the SE data. These more elaborate real-time SE models are left for development and implementation in future work.

This dual *in situ* system is advantageous for several reasons. The SE spectral range is appropriately chosen to effectively probe various optical transitions of transition metal oxide thin-films, which give insight into the electronic band structure and its real-time change. The *in situ* measurements are non-destructive and are free from sample degradation due to atmospheric surface-interface layers. Fast, simultaneous measurements performed by the RHEED and SE allow the entire thin-film growth process to be observed and characterized. Finally, even though a model analysis is a formidable task to obtain the optical parameters and dielectric functions of thin-films, the simultaneously obtained RHEED data can validate a model for SE analysis, which gives this system a significant advantage over physical vapor deposition systems featuring only a single *in situ* monitoring technique.

Chapter 3   Strain-induced metal-insulator transition in 3D SrIrO$_3$ thin films

Orthorhombic SrIrO$_3$ is a correlated metal whose electronic properties are highly susceptible to external perturbations due to the comparable interactions of spin-orbit interaction and electronic correlation. We have investigated the electronic properties of epitaxial orthorhombic SrIrO$_3$ thin-films under compressive strain using transport measurements, optical absorption spectra, and magneto-resistance. The metastable, orthorhombic SrIrO$_3$ thin-films are synthesized on various substrates using an epi-stabilization technique. We have observed that as in-plane lattice compression is increased, the dc-resistivity (ρ) of the thin films increases by a few orders of magnitude, and the dρ/dT changes from positive to negative values. However, optical absorption spectra show Drude-like, metallic responses without an optical gap opening for all compressively-strained thin films. Transport measurements under magnetic fields show negative magneto-resistance at low temperature for compressively-strained thin-films. Our results suggest that weak localization is responsible for the strain-induced metal-insulator transition for the orthorhombic SrIrO$_3$ thin-films.

3.1   Motivation

Perovskite SrIrO$_3$ is the three-dimensional end member of the Ruddlesden-Popper (R-P) series iridates, Sr$_{n+1}$Ir$_n$O$_{3n+1}$, whose electronic structure is tunable from a three-dimensional correlated metal, i. e. SrIrO$_3$ ($n = \infty$), to a two dimensional $J_{eff} = 1/2$ Mott insulator, i. e. Sr$_2$IrO$_4$ ($n = 1$) (41). The insulating state emerges when an octahedral crystal field splits the degenerate $5d$ levels into e_g and t_{2g} bands; the partially filled t_{2g} bands (L_{eff}

= 1) are further split into the J_{eff} = 3/2 and J_{eff} = 1/2 bands by the strong spin-orbit coupling inherent in iridium ions. The Mott gap opens in the J_{eff} = 1/2 band if the on-site Coulomb interaction becomes energetically comparable to or larger than the bandwidth. In $SrIrO_3$, there are six nearest neighbor Ir atoms, while in Sr_2IrO_4 there are only four. This reduction of coordination number of Ir $5d$ orbitals reduces the bandwidth and opens a gap in the partially filled J_{eff} = 1/2 band in Sr_2IrO_4. Hence, the metal-insulator transition in the R-P series iridates is driven by a *dimensionally controlled decrease in bandwidth*.

In this study, we have investigated whether a metal-insulator transition can also occur in epitaxial $SrIrO_3$ thin films via a strain-induced reduction in bandwidth. While the Ir-O bond length is rigid and difficult to change, the Ir-O-Ir bond angle can be readily affected by lattice strain (42,43). As schematically illustrated in Figure 3.1, when the Ir-O-Ir bond angle is decreased by compressive strain, the electronic hopping integral between Ir $5d$ orbitals is reduced, and hence the bandwidth decreases. This reduction in bandwidth can induce a metal-insulator transition either by opening a Mott gap, similar to Sr_2IrO_4 (41), or by creating a localized band below the mobility edge due to disorder (44). We have grown epitaxial $SrIrO_3$ (SIO) thin films on various substrates with close lattice mismatch. We find that as in-plane compression increases, the metallic SIO thin films become insulating. Optical absorption spectroscopy indicates that all SIO thin films have a metallic Drude-like response and lack the presence of an optical gap, despite the insulating transport behavior. Transport measurements under magnetic field display a negative magneto-resistance (MR) behavior in the insulating SIO thin films. Hence, the strain-induced metal-insulator transition is due to weak localization. Our results
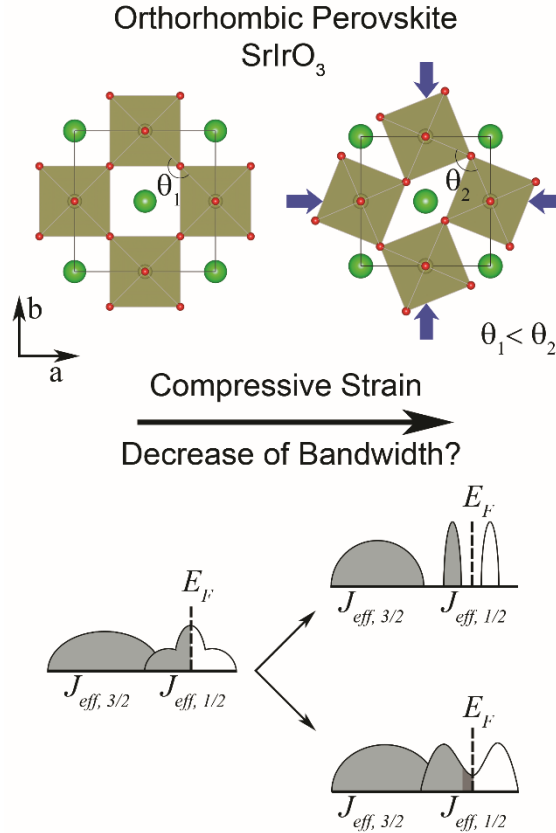
Figure 3.1: Schematic diagrams showing the relationship between compressive strain and bandwidth reduction. (top panel) In-plane compressive strain will cause the Ir-O-Ir bond angle θ to decrease. (bottom panel) By reducing the bandwidth, the correlated metallic band structure of SrIrO₃ (left) can turn insulating either by (upper) a Mott gap opening or (lower) localized states (emphasized in dark gray) forming below the mobility edge.

demonstrate that the electronic properties of perovskite SIO thin films can be manipulated

by compressive lattice strain.

3.2   Sample synthesis

We have grown orthorhombic SIO epitaxial thin films on several substrates with

various compressive strains using pulsed laser deposition. The thermodynamically stable

phase of bulk SIO crystals is the hexagonal 6H-BaTiO₃ structure at ambient conditions,

and the orthorhombic phase can be stabilized using a high-pressure synthesis (45,46).

However, orthorhombic SIO phases can be stabilized as epitaxial thin films on pseudo-

cubic perovskite substrates (47,48). Four single-crystal substrates are used: MgO (001),

GdScO$_3$ (110) (GSO), SrTiO$_3$ (001) (STO), and (LaAlO$_3$)$_{0.3}$(Sr$_2$AlTaO$_6$)$_{0.7}$ (001) (LSAT)

with in-plane pseudo-cubic lattice constants of 4.21, 3.96, 3.90, and 3.87 Å, respectively.

During the deposition, the substrate temperature is 700 °C in an oxygen partial pressure of

100 mTorr. The samples are post-annealed and cooled in a 1 Torr oxygen atmosphere.

Figure 3.2a shows θ-2θ X-ray diffraction data for all the SIO thin films used in this

study, and all thin films have the correct *00l* orientation with respect to the substrate

normal. As the in-plane lattice parameters are decreased from MgO to LSAT, the *00l* thin

film peaks are shifted to lower angles, indicating an out-of-plane (*c*-axis) expansion of the

SIO unit cell. This is consistent with an in-plane compressive strain causing an elongation

along the *c*-axis. The SIO thin film thicknesses are found to be around 20 nm using X-ray

reflection fringes. The rocking curves in Figure 3.2b are taken of the *002* film reflection.

The thin films grown on GSO, STO, and LSAT have full widths at half maximum less than

0.08°, indicating high crystallinity. X-ray reciprocal space maps of the (pseudo-cubic)

103-reflection in Figure 3.2c show the SIO thin films on GSO, STO, and LSAT are

coherently strained. As the compressive strain increases from GSO to LSAT, the 103 film

reflection shifts downward, which is consistent with the θ-2θ scans in Figure 3.2a. The

SIO thin film on MgO is relaxed due to the large lattice mismatch ($\sim$5%), and this sample

is expected to emulate properties of unstrained ('bulk') SIO. The lattice parameters are

found using the reciprocal space reflection peaks ($Q_i = 2\pi/d_{hkl}$, where $i \equiv \perp$ or // and d_{hkl} is

the spacing between appropriate reflection planes (*hkl*)). Figure 3.2d shows the change of
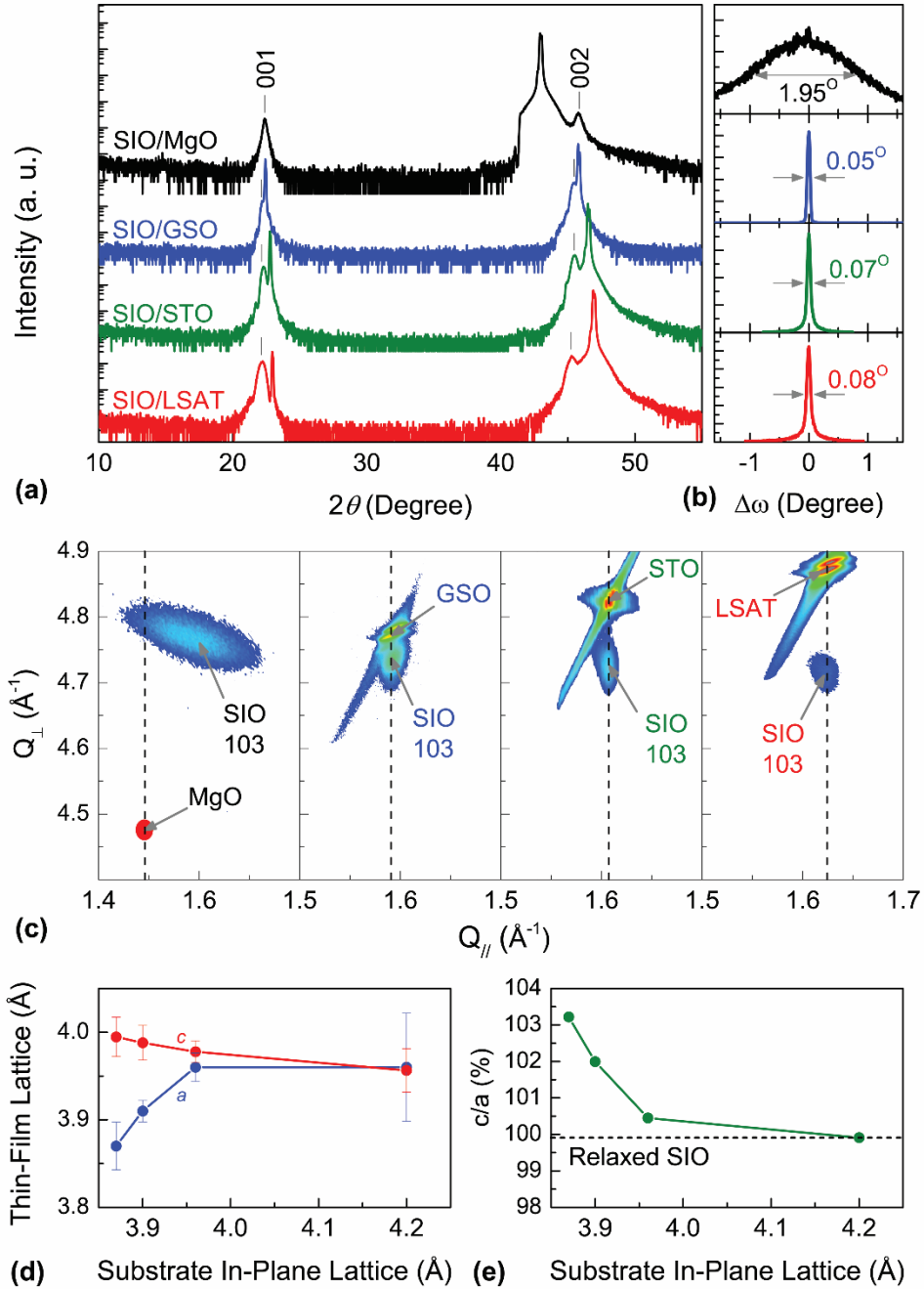
Figure 3.2: X-ray diffraction scans confirming the epitaxial growth of perovskite SIO thin films. The films are grown on MgO (black), GSO (blue), STO (green), and LSAT(red): (a) θ-2θ diffraction scans show correct *00l* oriented film peaks, (b) rocking curve $\Delta\omega$ scans about the film's 002-reflection, and (c) reciprocal space maps around the 103-reflection (pseudo-cubic notation) of the substrates. (d) The out-of-plane *c* and in-plane *a* lattice constants of the strained SIO thin films and (e) the ratio *c/a* as a function of substrate in-plane lattice.

in-plane (*a*) and *out-of-plane* (*c*) lattice parameters as a function of the substrate in-plane

lattice constant. The ratio *c/a* quantifies the tetragonal distortion due to strain present in the SIO thin films, with *c/a > 100%* corresponding to compressive strain. Figure 3.2e shows the thin films grown on LSAT, STO, and GSO are compressively strained with a tetragonal distortion, and the SIO thin film on MgO is relaxed with a cubic structure.

3.3　Transport properties

Figure 3.3 shows temperature dependent resistivity curves $\rho(T)$, which indicate a large dependence on compressive lattice strain. The resistivity of each strained SIO thin film systematically increases with in-plane compression. The resistivity of the SIO films are of the same order of magnitude as the resistivity measured in a polycrystalline, high pressure synthesis study of SIO (~ 2 mΩ cm at room temperature) and other SIO thin film
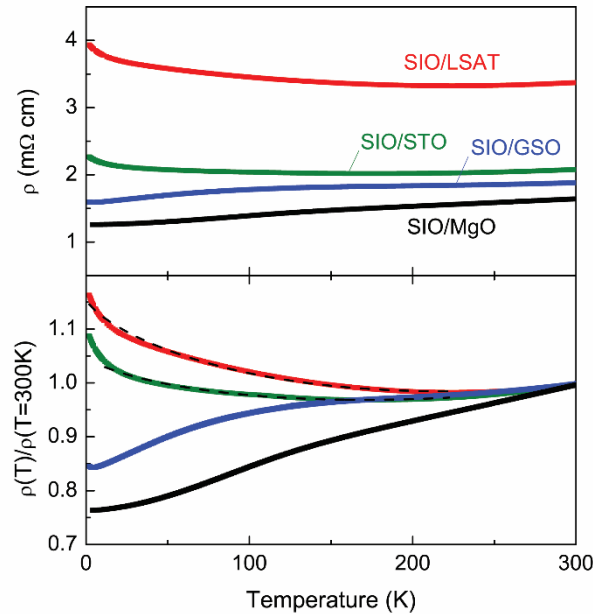
Figure 3.3: Resistivity versus temperature (upper panel) of SIO films grown on MgO, GSO, STO, and LSAT substrates. The resistivity increases with in-plane compression. The room-temperature normalized resistivity (bottom panel) clearly shows the strain-dependence of the transport, and the insulating regions of SIO on STO and LSAT are fit (dashed lines) with a weak localization model (see Equation (3.1)).

studies (46,49-51). In addition to an increase in resistivity, the SIO films synthesized on

27

STO and LSAT have an upturn in their resistivity curves at 175 K and 225 K, respectively. The room temperature-normalized resistivity curves are shown in the bottom panel of Figure 3.3. The resistivity of the relaxed SIO on MgO has a positive slope ($d\rho/dT$) for all temperatures from 4 to 300 K, which is expected for metallic behavior. The positive slope is reduced for the thin film grown on GSO and becomes increasingly negative for the thin films grown on STO and LSAT. To gain a phenomenological understanding of the insulating regions, resistivity data (< 225 K) of SIO grown on STO and LSAT are fit with:

$$\rho = \rho_0 - \alpha T^{3/4} + \beta T^{\frac{3}{2}} \qquad (3.1)$$

where $\rho_0, \alpha,$ and β are the fit parameters for remnant resistance, three dimensional weak localization and inelastic scattering due to electron-boson interactions, respectively (52,53). Weak localization is a disorder driven effect due to quantum interference of the conducting charge carriers at defect sites (54). The weak localization coefficient α for the SIO thin film on LSAT is twice as large as the fit coefficient for the thin film grown on STO, as shown in Table 3.1. Based on the lattice parameters obtained from the X-ray diffraction data, the compressively strained SIO thin films are not oxygen deficient, eliminating a potential source of defect scattering. Although further experimental characterizations are needed to fully understand the defects, one possible mechanism is misfit dislocations caused by compressively straining the SIO films, which would lead to weak localization. The exact physical origin should be explored in future studies. This weak-localization model fit is similar to a previous study of compressively strained SIO perovskite films of similar thickness grown on $LaAlO_3$ substrates (53).

Table 3.1: SIO thin film summary: tetragonal distortion $(\frac{c}{a})$ from reciprocal space maps; weak localization $\frac{\alpha}{\rho_0}$ and electron-boson scattering $\frac{\beta}{\rho_0}$ fit parameters from transport; and plasma frequency ω_p, interband absorption $\omega_{o,\beta}$, and carrier density n from Drude-Lorentz fit of absorption spectra.

Substrate	c/a	Transport		Absorption Spectra		
		α/ρ_0	β/ρ_0	ω_p	$\omega_{o,\beta}$	n
	(%)	$(K^{-3/4})$	$(10^{-5}\ K^{-3/2})$	(eV)	(eV)	$(10^{22}\ cm^{-3})$
MgO	100	-	-	10	0.91	7.7
STO	102	0.003	3.66	7.4	0.79	4.0
LSAT	103	0.006	5.33	2.6	0.79	0.49

3.4   Optical properties

Optical absorption spectroscopy provides insight into understanding the electronic band structure and free carrier dynamics of thin films. It also offers a method of determining the insulating gap energy by measuring the photon energy of zero absorption coefficient. Optical transmission spectra $T(\omega)$ of our samples are taken at room temperature using a Fourier-transform infrared spectrometer (for spectra regions between 50 meV – 0.6 eV) and a grating-type spectrophotometer (for spectra regions between 0.5 – 6 eV). This spectral range is sufficient for measuring transmittance spectra down to the Reststrahlen band of each respective substrate, which is the lowest energy limit for transmission spectra. The optical absorption spectra $\alpha(\omega)$ of SIO thin films are obtained
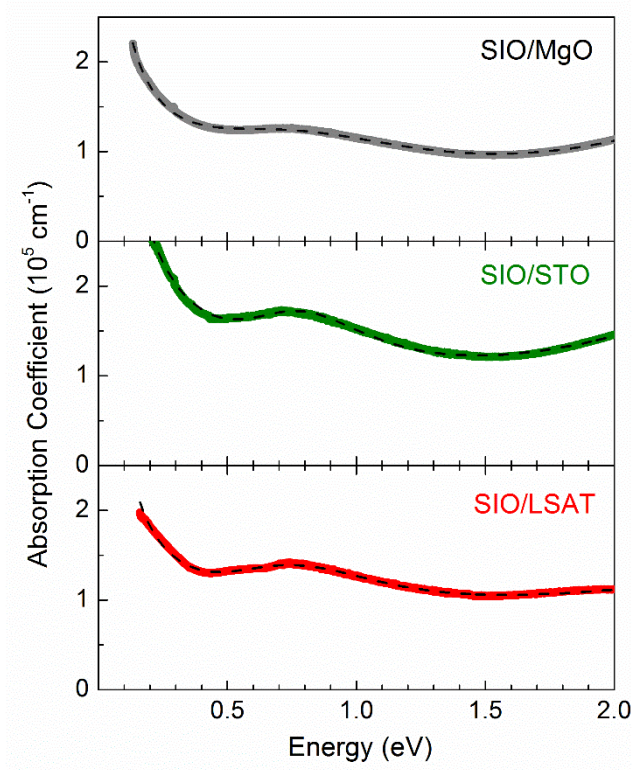
Figure 3.4: Optical absorption spectra of SIO films grown on MgO, STO, and LSAT substrates. The dashed black lines are Drude-Lorentz fits using the Drude model and two Lorentz oscillators: for the interband β absorption (~0.8 eV) and for the charge transfer.

using $\alpha(\omega) = -\frac{1}{t}\ln[T(\omega)_{film+substrate}/T(\omega)_{substrate}]$, where t is the thin film thickness. According to Fermi's golden rule, $\alpha(\omega)$ is proportional to the product of the transition probability amplitude and joint density of states. Therefore, the ith interband-transition peak position $\omega_{0,i}$ in $\alpha(\omega)$ corresponds to the energy difference between bands, and the corresponding peak width γ_i is proportional to the bandwidth. SIO thin films grown on MgO and GSO substrates are known to show a Drude-like response at energies in the infrared, an interband optical transition $\omega_{o,\beta} \sim 0.8\ eV$ from the $J_{eff} = 3/2$ band to the $J_{eff} = 1/2$ band, and a higher energy charge transfer from O $2p$ bands to Ir $5d$ bands (41,50).

Despite the compressively strained thin films having a negative dρ/dT behavior, the absorption spectra in Figure 3.4 show all the SIO films have a Drude-like response at low

energies, which suggests a metallic behavior. The absorption coefficient $\alpha(\omega)$ is proportional to the extinction coefficient k by $\alpha(\omega) = \frac{2k\omega}{c}$, which is nonlinearly related to the dielectric function by: $k = \sqrt{\frac{1}{2}(\sqrt{\varepsilon_1 - \varepsilon_2} - \varepsilon_1)}$, where c is the speed of light and ε_1 and ε_2 are the real and imaginary parts of the complex dielectric function, respectively. The absorption spectra for all samples are fit to the Drude model for the low energy metallic response, a Lorentz oscillator for the interband β transition, and a second Lorentz oscillator for the higher energy charge transfer transition.

In the Drude model, the complex dielectric function is given by $\tilde{\varepsilon}_{Drude}(\omega) = \varepsilon_1 + i\varepsilon_2 = 1 - \frac{\omega_p}{\omega^2 + i\omega\gamma}$, where the two fit parameters are the plasma frequency ω_p and the scattering rate γ. As summarized in Table 3.1, the free charge carrier density n for each SIO film is found using $\omega_p = (n\,e^2/(m^*\varepsilon_0))^{\frac{1}{2}}$, where e is the elementary charge, m^* is the effective mass of an electron, and ε_0 is the permittivity of free space. S. J. Moon *et al.* reported a frequency-dependent mass enhancement of SIO's conducting carriers only at low energies, and the effective mass approaches the free electron mass m_e around 0.08 eV (41). Therefore, in our spectral range (> 0.2 eV) it is assumed $m^* = m_e$, and the free charge density n is found to be $7.7 \times 10^{22}\ cm^{-3}$, $4.0 \times 10^{22}\ cm^{-3}$, and $4.9 \times 10^{21}\ cm^{-3}$ for SIO grown on MgO, STO, and LSAT, respectively. Although both compressively strained SIO films feature insulating properties, all films have free carrier concentrations of the same order of magnitude, albeit smaller than that of most metals. The carrier density of SIO on MgO is also verified using a room temperature Hall measurement and is found to be $7.3 \times 10^{22}\ cm^{-3}$, which is in agreement with the n found in the optical spectra and supports the assumption $m^* = m_e$. The absorption peak $\omega_{o,\beta}$ around *0.8 eV* remains

relatively constant for all SIO films; however, the peak width γ_β of the relaxed SIO on MgO is larger than γ_β of each compressively strained film on STO and LSAT. This is consistent with the expectation of in-plane compressive strain causing a decrease in the Ir-O-Ir bond *angle* and therefore decreasing the bandwidth, albeit not large enough to open an insulating band gap. If the Ir-O bond *length* had decreased in compressively strained SrIrO₃ films, the peak widths would increase and conduction would be enhanced, which is opposite to the behavior observed in our thin films. Therefore, the Ir-O-Ir bond *angle* rather than the Ir-O bond length in SrIrO₃ thin films is more energetically favorable to alter by epitaxial, compressive strain.

3.5   Magneto-resistance measurements

The SIO thin films grown under compressive strain (on STO and LSAT) exhibit a negative magneto-resistance (MR) behavior at low temperatures while the MR of the SIO thin film grown on MgO shows a positive B^2 behavior [MR (%) $= 100 \times \frac{R(B)-R(0)}{R(0)}$, where $R(0)$ and $R(B)$ are thin film resistance for zero and non-zero magnetic field B, respectively]. For each sample, the MR response is qualitatively isotropic in the following field and thin film orientations: $B \parallel c, B \perp I$ (Figure 3.5) and $B \perp c, B \perp I$, where I is the in-plane current and c is the out-of-plane film axis. The positive B^2 MR is typical for simple metals and is observed for the unstrained SIO on MgO. The negative MR for the compressively strained thin films grown on STO and LSAT is consistent with the data reported in Ref. (53). The MR data supports the picture in Figure 3.1 that weak localization causes the insulating behavior of compressively strained SIO thin films. For weak localization, time reversal symmetry must be preserved. By applying magnetic fields, a phase shift occurs in the electronic wave functions. Hence, this asymmetrical phase shift

between forward and backscattered electrons suppresses the interference, i.e. weak localization, and results in a decrease in the resistance under magnetic fields, which is a negative MR behavior (54).

3.6   Summary

Epitaxial SrIrO₃ thin films have been synthesized on various substrates inducing in-
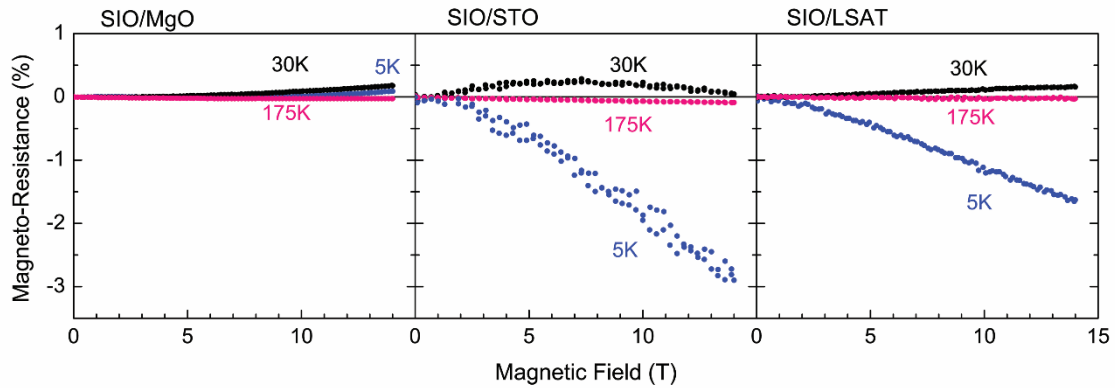
Figure 3.5: Magneto-resistance (MR) versus magnetic field taken at 5 K, 30 K, and 175 K for SIO films grown on MgO, STO, and LSAT. The SIO on MgO displays typical metallic B^2 behavior. The compressively strained films grown on STO and LSAT have negative MR, supporting weak localization.

plane compressive strain and film relaxation. Relaxed SIO is metallic for all temperatures while the strained thin films have an increase in their resistivity as a function of compression. Weak localization corrections are fit to the resistivity curves of the SIO thin films with insulating properties. Although the compressively strained films exhibit insulating properties, the optical absorption spectra of all SIO thin films have a Drude-like metallic response at low energies. The $J_{eff} = 3/2$ absorption peak is centered around 0.8 eV, and the bandwidth decreases with in-plane compressive strain. This implies that compressive strain induces an in-plane rotation of the oxygen octahedra causing a decrease in bandwidth, but fails to open an insulating bandgap. The positive, quadratic MR for the relaxed SIO film is typical for metals, and the negative MR of the compressively strained

films is indicative for insulating samples due to weak localization. As schematically summarized by Figure 3.1, these results demonstrate the effect of lattice strain on the electronic structure of SIO, and the role of weak localization in obtaining insulating states in strongly correlated, metallic systems. This offers an important progression in our understanding of similar *5d* transition metal oxide systems and heterostructures with strong spin-orbit coupling and electron correlation.

Chapter 4   Creating 1D quantum stripes from 2D layered materials

One-dimensional (1D) quantum systems, which are predicted to exhibit novel states of matter in theory, have been elusive in experiment. In this study, we develop a superlattice method of creating artificial 1D quantum stripes, which offers dimensional tunability from two- to one-dimensions. As a model system, we have fabricated 1D iridium (Ir) stripes using *a-axis oriented superlattices* of a relativistic Mott insulator Sr_2IrO_4 and a wide bandgap insulator $LaSrGaO_4$, both of which are crystals with layered structure. In addition to the successful formation of 1D Ir-stripe structure, we have observed 1D quantum-confined electronic states from optical spectroscopy and resonant inelastic x-ray scattering. Since this 1D superlattice approach can be applied to a wide range of layered materials, it opens a new era of 1D science.

4.1   Motivation of study

An ideal one-dimensional quantum-stripe consists of an infinite linear chain of bonded atoms, wherein the interactions between each atom's electrons are restricted to the single dimension of the chain (55). One-dimensional (1D) order spontaneously emerges at the onset of quantum phase transitions in the form of charge/spin density waves in multiferroics, superconductors, and as edge and surface states in topologically non-trivial systems (56-62). An experimental approach for investigating such phenomena is to dimensionally tune these systems to one dimension until a critical phase transition is reached, as conducted similarly in Ruddlesden-Popper series compounds from three to two dimensions (1). While many successful strategies have been demonstrated for chemically synthesizing 1D nanostructures, direct atomic-layer control between two and one

dimension(s) is generally considered unavailable (63). Additionally, the quantum confinement of conventionally two dimensional materials to one dimension can reveal hidden electronic and magnetic properties. For example, $SrCuO_2$, i.e. 1D chain compound, shows novel spin-charge separation, which is absent in its 2D counterpart, $Sr_2CuO_2Cl_2$ (Ref. (64)). Despite the promising outlook for 1D materials, experimental progress remains in its infancy, hampered by its reliance on the few materials with intrinsic 1D structure (65).

4.2   Methodology of 1D stripe synthesis

In this new approach of synthesizing 1D quantum systems, dimensionally-confined stripe-superlattices are constructed from *in-plane* oriented 2D layered crystals. Layered transition metal oxides of the form A_2BO_4 consist of 2D layers (BO_2) in the *ab*-plane that are stacked along the *c*-axis. Such materials are considered 2D since each consecutive plane is well separated by an electronically inert rock salt layer (AO) and offset by a half unit cell. Compounds with this K_2NiF_4-type structure can be epitaxially grown such that the 2D layers are oriented parallel to the surface normal direction, i.e. *a*-axis orientation (66-68). The crux of our idea is that the dimensionality of the 2D layered materials in this *a*-axis orientation can be tuned by restricting the number of monolayers m grown along the *in*-plane direction (Figure 4.1a). For instance, if only a single monolayer is grown, i.e. $m = 1$, then the 2D planes become 1D stripes. To achieve a volume suitable for experimental characterizations, superlattice structures can be grown consisting of alternating layers of m monolayers of BO_2 and n monolayers of an inert, wide bandgap material also containing the K_2NiF_4 symmetry ($A'_2B'O_4$). In this manner, the 2D planes can be incrementally tuned to 1D quantum stripes.
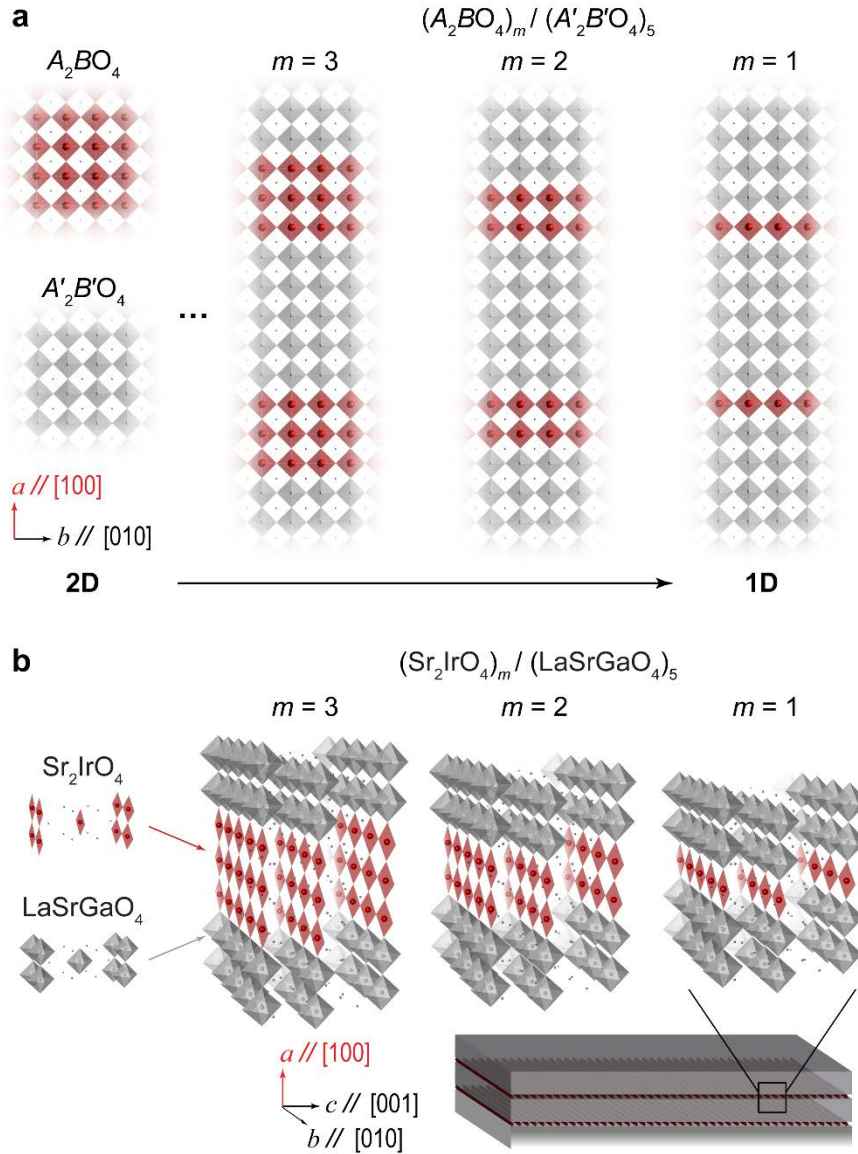
Figure 4.1: Conceptual diagram of turning a 2D layered material into a 1D quantum stripe superlattice. a) The leftmost panel shows the in-plane structures of two transition-metal oxides, A_2BO_4 (above) and $A'_2B'O_4$ (below), with the K_2NiF_4 symmetry. Each red (gray) square contains transition-metal ions B (B') at its center and an oxygen atom at each of its 4 vertices. The number of BO_2 monolayers m corresponds to the horizontal rows of red squares, i.e. the stripes. Low-dimensional stripe phases approaching 1D (e.g. $m = 3, 2, 1$) can be created by alternating the layers between m monolayers of BO_2 and a constant number of $B'O_2$ monolayers (such as 5 in the schematic). The 1D quantum-stripes are achieved in the $m = 1$ case depicted in the rightmost panel. b) Schematic diagrams of a-axis oriented $(Sr_2IrO_4)_m/(LaSrGaO_4)_5$ superlattices for $m = 3$, $m = 2$ and $m = 1$ for realizing the low-dimensional quantum stripes of IrO_2 (red squares) on $LaSrGaO_4$ (100) substrates. The 1D IrO_2 stripes run parallel to the b-axis and are dimensionally confined by the wide bandgap $LaSrGaO_4$ layers (grey octahedra).

We have implemented this idea in synthesizing 1D IrO_2 stripes using *in*-plane

oriented superlattices of Sr$_2$IrO$_4$ and the wide bandgap insulator LaSrGaO$_4$ (E_g = 3.8 eV) (Figure 4.1b and Figure 4.2). We have used *a*-axis oriented LaSrGaO$_4$ (100) as both the substrate and insulating sublayers. The samples in this study are 30 superlattice-unit-cells thick, and each superlattice unit cell consists of *m* monolayers of Sr$_2$IrO$_4$ and 5 monolayers of LaSrGaO$_4$. To synthesize the 1D superlattice structures, we have used our customized pulsed laser deposition (PLD) system in order to optimize monolayer-controlled deposition of Sr$_2$IrO$_4$ and LaSrGaO$_4$ (see Ref. (69) for detailed growth methods). For a monolayered controlled growth, it is important to maintain a slow growth rate of Sr$_2$IrO$_4$ and LaSrGaO$_4$ layers, ca. 200 laser pulses per monolayer. The growth parameters of the deposition require an oxygen partial pressure (P$_{O2}$) of 10 mTorr, a substrate temperature of 700 ˚C, and laser (KrF excimer, λ = 248 nm) fluence of 1.2 J/cm^2. The superlattice growth is monitored
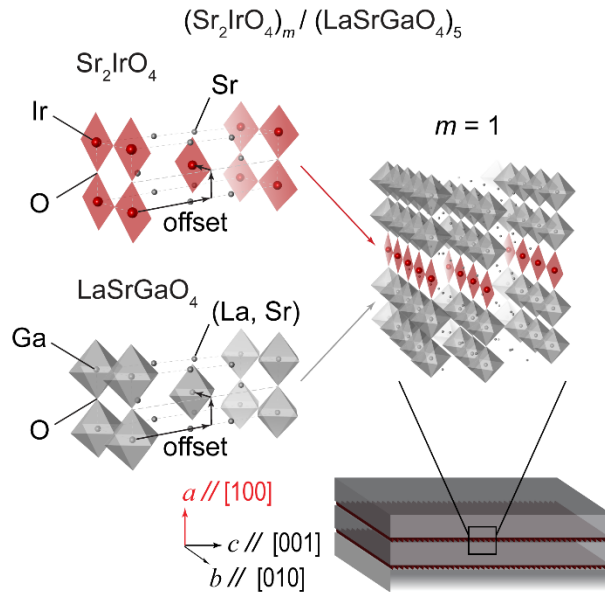
Figure 4.2: Schematic detailing the atomic and geometric configurations of Sr$_2$IrO$_4$ and LaSrGaO$_4$ unit cells. The 2D planes in Sr$_2$IrO$_4$ and LaSrGaO$_4$ consist of an array of octahedra, which each corner-share oxygen atoms in the *ab*-plane and centrally contain the transition metal Ir or Ga, respectively. The 2D planes are each separated by a rock salt layer of SrO for Sr$_2$IrO$_4$ and (La,Sr)O for LaSrGaO$_4$, and adjacent planes are each offset by a half unit cell. For our 1D *m* = 1 structure, one monolayer (a half unit cell) of Sr$_2$IrO$_4$ is deposited along the *a*-axis followed by 5 monolayers (four and a half unit cells) of LaSrGaO$_4$.

38

using RHEED (see *Figure 4.3*), and the deposited monolayers of both LaSrGaO$_4$ and Sr$_2$IrO$_4$ show distinct axis-dependent diffraction patterns during the entire deposition, which indicate the proper structural confinement required for creating the 1D IrO$_2$ stripe-structures.
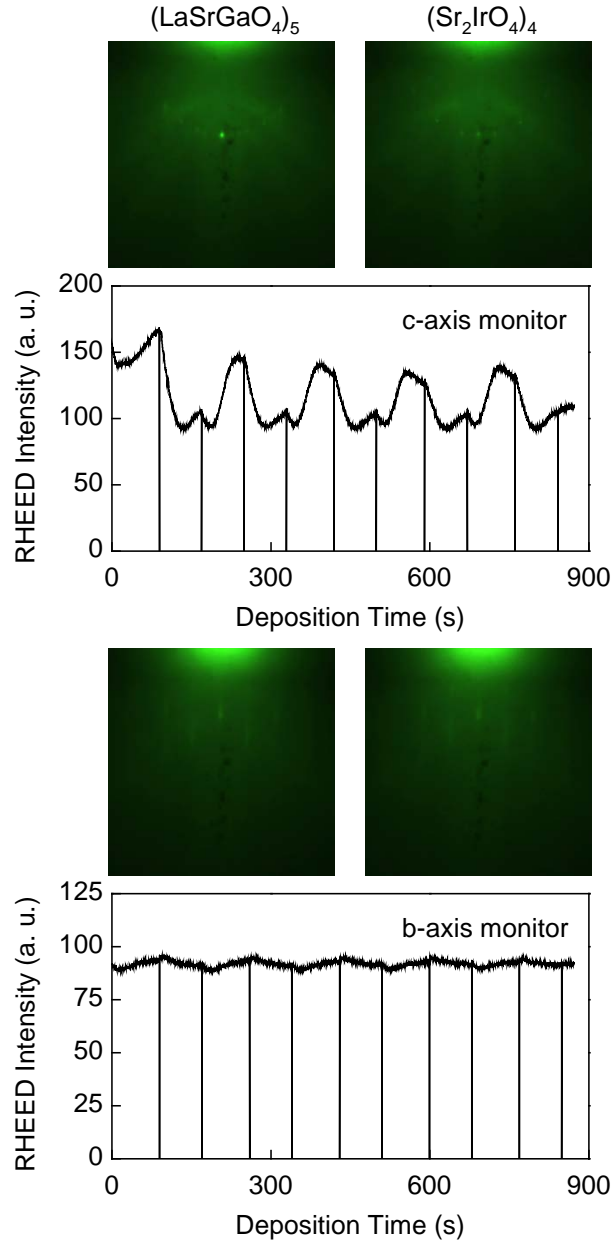
Figure 4.3: RHEED monitor during $m = 4$ growth. The in-plane anisotropy of the (Sr$_2$IrO$_4$)$_4$/(LaSrGaO$_4$)$_5$ superlattice induces distinct axis dependent RHEED diffraction patterns and intensity fluctuations for monitoring the c-axis (top panel) and b-axis (bottom panel). The RHEED intensity and diffraction patterns remain relatively stable, indicating the superlattice retains structural integrity during the deposition.

While there have been many previous investigations on the unique spin-orbit coupled $J_{eff} = 1/2$ Mott insulating state present in the 2D layered iridate Sr_2IrO_4 (70-73), there are no previously studied or discovered 1D iridate systems to date. Recent studies on 2D Sr_2IrO_4 also have revealed interesting phenomena such as the presence of excitonic quasiparticles and indications of new superconducting ground states for doped samples (74-77). Using structural and electronic characterizations of x-ray diffraction, high-resolution scanning transmission electron microscopy (STEM), optical spectroscopy, and resonant inelastic x-ray scattering, we have confirmed that both 1D structural and electronic confinement is achieved for this system. Our experimental observations are also consistent with the calculations of density functional theory. These results imply that this method can be extended to any 2D layered material and thereby allow for tunability to 1D quantum structures previously disregarded in experimental one-dimensional science.

4.3   Structural evidence of 1D confinement

The 1D stripe-structures of our superlattice samples have been confirmed by x-ray diffraction and high-resolution STEM. *Figure 4.4*a shows clear periodic superlattice peaks in the 2θ-ω x-ray diffraction scans. Since each superlattice unit cell consists of m monolayers of Sr_2IrO_4 and 5 monolayers of $LaSrGaO_4$, i.e. $(Sr_2IrO_4)_m$/$(LaSrGaO_4)_5$ ($m = 1 - 5$), the superlattice diffraction peak periodicity Δh shows excellent agreement to $1/(m + 5)$. For strain information, x-ray reciprocal space maps have been taken near the (310)- and (303)- reflections of $LaSrGaO_4$ for the ab- (*Figure 4.4*b) and ac-planes (*Figure 4.4*c), respectively. The vertical alignment of the superlattice peaks with the substrate reflections indicates all superlattices are coherently strained along both directions, i.e. b- and c-axes.
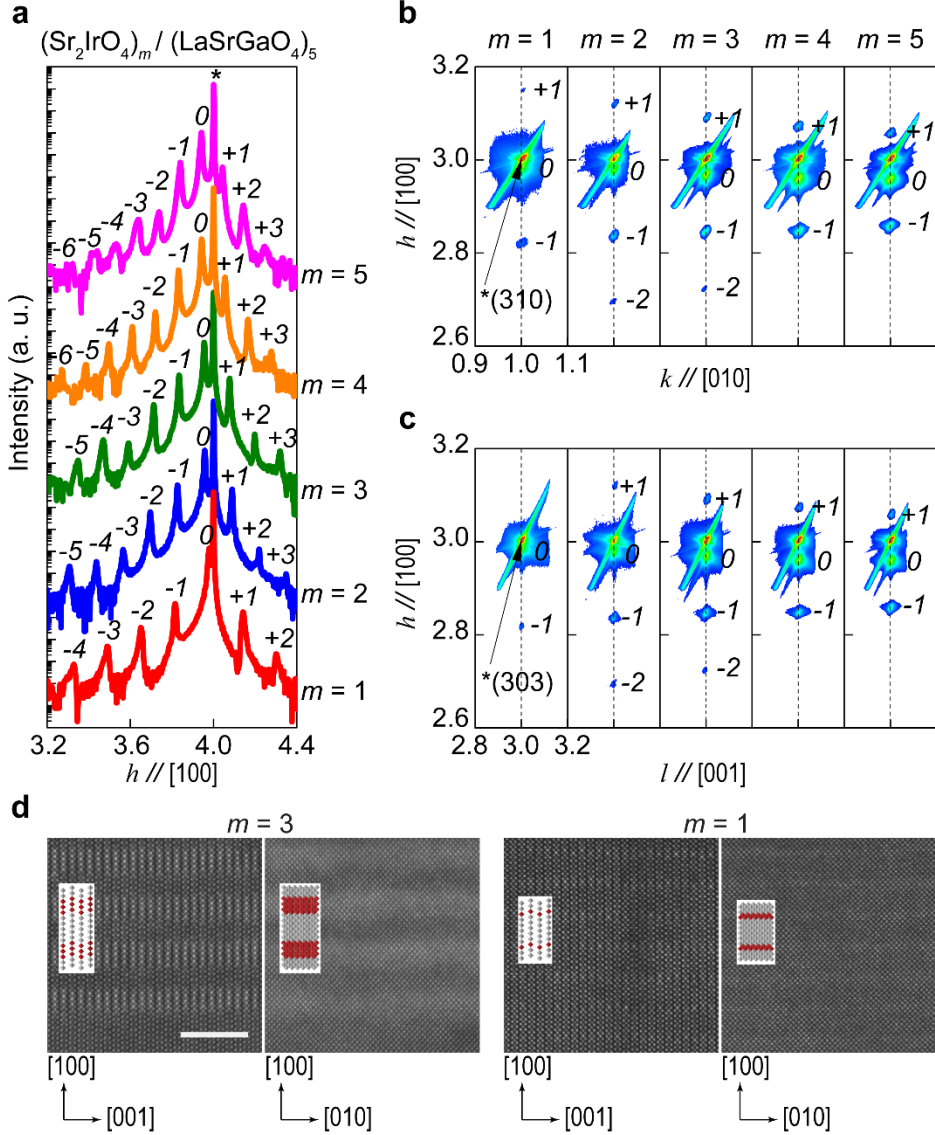
Figure 4.4: X-ray diffraction scans and Z-contrast STEM data of $(Sr_2IrO_4)_m/(LaSrGaO_4)_5$ superlattices. a) 2θ-ω x-ray diffraction scans of $(Sr_2IrO_4)_m/(LaSrGaO_4)_5$ superlattices (labeled accordingly to the right). The $LaSrGaO_4$ (400)-diffraction peaks are indicated by an asterisk (*). The central superlattice peak is the zeroth order Bragg diffraction peak (indexed as *0*), and the superlattice satellite peaks are indexed relative to this peak. Two x-ray reciprocal space maps are taken for each superlattice sample about b) the (310)- and c) the (303)-reflections of $LaSrGaO_4$ (*) to obtain complete in-plane strain information. d) Z-contrast STEM images of $m = 3$ (left pair) and $m = 1$ (right pair) superlattices. Two cross-sections are shown for each sample: the *ac*-plane (left scan of each pair) and the *ab*-plane (right scan of each pair). The brightest dots are Ir ions and the inset schematics employ the same color scheme as in Figure 4.1b. Note that the IrO_2 stripes run along the *b*-axis ([010]-direction), that is the out of page direction in the left image and the horizontal direction in the right image of each sample. All images have the same scale bar (leftmost image) of 5 nm.

STEM further confirms that the 1D superlattice structures are successfully formed (*Figure*

41

*4.4*d). The expected half-unit cell offset (zig-zag shape) and Sr-O rock salt separation between neighboring IrO_2 stripes along the *c*-axis is readily apparent in the *ac*-plane scans of the *m* = 3 and *m* = 1 samples. Along the *b*-axis, the IrO_2 stripes are coherent; however, the stripe boundaries in this planar view are rather indeterminate due to the inter-stripe half unit cell offset between each planar layer. These observations provide convincing evidence for the successful creation of 1D IrO_2 stripe-structures from the 2D Sr_2IrO_4.

4.4   Electronic confinement of 1D stripes

Linearly polarized optical spectroscopy shows clear anisotropic characteristics and 1D electronic confinement of the stripe-structures. The directional-dependent absorption spectra are obtained by linearly polarizing the incident photons such that the electric field *E* is perpendicular (parallel) to the 1D IrO_2 stripe direction along the *b*-axis, as shown by the graphic in *Figure 4.5*a (*Figure 4.5*b). The optical conductivity spectra (σ_1 (ω)) are obtained by taking a Kramers-Kronig transformation of the absorption spectra α (ω) (Figure 4.6) and are normalized by the number of Ir monolayers per superlattice unit cell, i.e. $m/(m + 5)$ for the $(Sr_2IrO_4)_m$ /$(LaSrGaO_4)_5$ superlattices. When the polarization is parallel to the 1D IrO_2 stripe direction, i.e. *E* // *b* (Figure 4.5b), there are broad peaks in the optical spectra. The finite peaks appear due to the Ir-Ir inter-site optical transitions in the J_{eff} = 1/2 band (75,78,79). Note that the peaks are significantly reduced (Figure 4.5a) when the polarization is perpendicular to the IrO_2 stripe direction, i.e. $E \perp b$. If the IrO_2 stripes are truly 1D, this can be understood intuitively since no Ir-Ir inter-site optical transitions are possible perpendicular to the *b*-axis. Hence, the observation of optical anisotropy confirms that the 1D IrO_2 stripes are also confined *electronically*. As *m* decreases, i.e. the samples approach one dimension, the spectral weight in the absorption is reduced (Figure
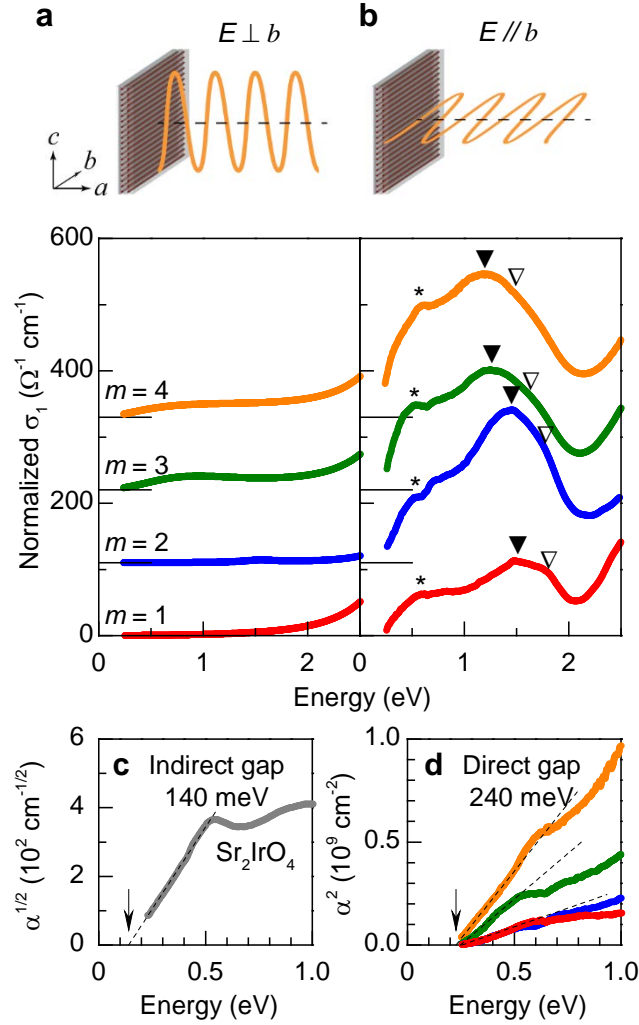
Figure 4.5: Optical spectra of $(Sr_2IrO_4)_m/(LaSrGaO_4)_5$ superlattices. Above each plot, an experimental depiction of the two sets of incident photons with linear polarization (E) a) perpendicular and b) parallel to the IrO_2 stripe-direction (b-axis) for $m = 1$ (red), 2 (blue), 3 (green), and 4 (orange) superlattices. All optical conductivity spectra σ_1 are normalized by the number of Ir monolayers per superlattice unit cell for comparison, and $m = 2$, 3, and 4 spectra are vertically shifted for clarity. The strong optical anisotropy, i.e. the absence of the low energy absorption peaks when E is perpendicular to the 1D IrO_2 stripes, confirms the low-dimensional electronic confinement. In the $m = 4$ superlattice spectra, the two peaks indicated by * and ▼ closely match the peak positions of 2D Sr_2IrO_4 crystals. As the dimensionality decreases, several notable features include: the change in electronic band and optical gap nature from c) an indirect gap (band edge linear with $\alpha^{1/2}$) to d) a direct gap (band edge linear with α^2), the appearance of van Hove singularities, the distinct emergence of a higher energy peak marked by ▽, and a blue-shift of the ▼ peak.

4.6) and the indirect gap observed in 2D Sr_2IrO_4 (Figure 4.5c) becomes a direct gap for the

1D superlattices (Figure 4.5d). New sharp features also appear in the spectra (marked as

∇ in Figure 4.5b). The sharp features present in the optical spectra are attributed to van Hove singularities, the appearance of which is contingent upon the low dimensionality of the crystal (80). The low dimensionality also contributes to an enhanced effective electron-correlation U_{eff}, which is responsible for the blue-shift of the optical transitions (Figure 4.6).
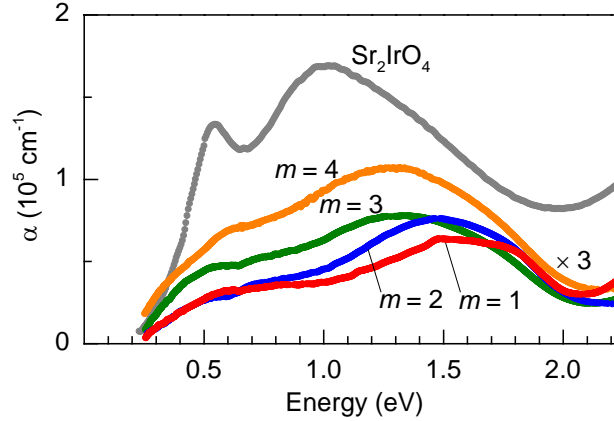
Figure 4.6: Linearly polarized optical absorption spectra of $(Sr_2IrO_4)_m/(LaSrGaO_4)_5$ superlattices ($m = 1 - 4$). The absorption spectra are taken at normal incidence and polarized such that the AC electric field E is parallel to the IrO_2 stripe direction (*b*-axis), as schematically depicted in Figure 3b. In comparing with Sr_2IrO_4 (grey), the superlattice absorption monotonically decreases as 1D is approached from $m = 4$ to $m = 1$, and the blue shift of the central absorption peak is also readily apparent. For visual clarity, the absorption spectra for *m = 1, 2, 3, 4* have been multiplied by a factor of three.

In order to reveal the elementary excitation dynamics of spin/orbital degrees of freedom exhibited by the 1D IrO_2 stripe-structures, we have taken resonant inelastic x-ray scattering (RIXS) spectra (For measurement geometry, see Figure 4.6). In the case of 2D Sr_2IrO_4, RIXS spectra reveal a magnon produced by antiferromagnetic Heisenberg spin below 0.2 eV as well as dispersive excitonic quasiparticles of J_{eff} orbitals (spin-orbit excitons) above 0.4 eV (Figure 4.7a and Ref. (74)). For the 1D superlattice, the $m = 1$ RIXS spectra reveal many unique features not present in its 2D Sr_2IrO_4 counterpart (Figure
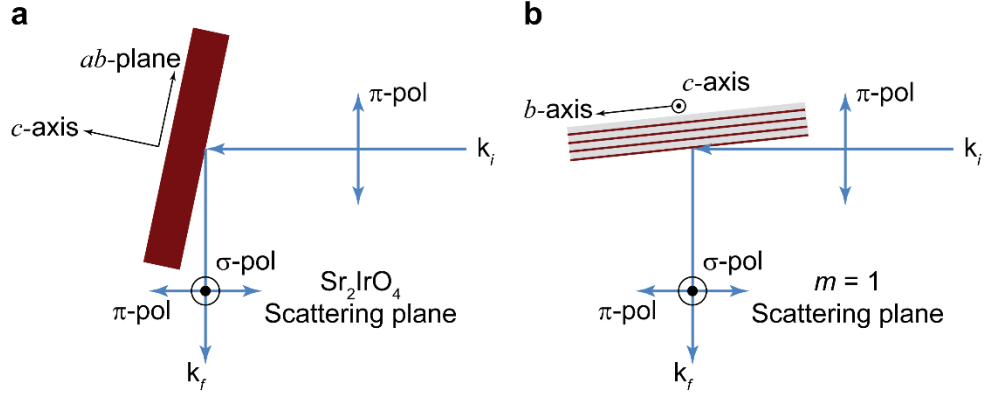
Figure 4.7: Measurement geometry of resonant inelastic scattering measurements (RIXS) with respect to Sr_2IrO_4 and the 1D $m = 1$ superlattice. The incident-photon is polarized along a) the ab-plane for bulk Sr_2IrO_4 and along b) the a-axis for the 1D $m = 1$ superlattice. The scattered-photon polarization has components both parallel to the incident polarization (π-polarization) and perpendicular to the scattering plane (σ-polarization). In this geometry, the in-plane spin components (*ab*-plane of bulk Sr_2IrO_4 and *b*-axis of the 1D *m* = 1 superlattice) and the out-of-plane spin components (*ab*-plane of bulk Sr_2IrO_4 and *c*-axis of 1D *m* = 1 superlattice) are probed. The scattered-photon polarization is used to probe the orbital lobes of the *c*-axis and in-plane directions for both samples. The geometry in a) is used to maximize the RIXS matrix elements for the transition between $|J_{eff} = 1/2, J_z = 1/2\rangle$ $(= |xy,+\rangle + |yz,-\rangle + i|zx,-\rangle)$ and $|J_{eff} = 3/2, J_z = \pm 3/2\rangle$ $(=|yz,\pm\rangle \pm i|zx,\pm\rangle)$. The resolution-limited orbital exciton peak at 600 meV of the 1D *m* = 1 superlattice can be assigned as from the same orbital transition. The same energy resolution of 30 meV is used for both measurements, and incident- and scattered-photon polarizations are also similar in both cases.

4.7b and Figure 4.7c). The spin excitation energy of the 1D IrO_2 stripes (~0.2 eV) is higher than that of 2D Sr_2IrO_4 (~0.06 eV), which implies that the 1D IrO_2 stripes have higher exchange interactions due to the localized character of the 1D spin structure. In the region of orbital excitations, a resolution-limited spin-orbit exciton at 0.6 eV is discovered. This is interpreted as arising from the same J_{eff} orbital transitions of the spin-orbit exciton in bulk Sr_2IrO_4— with a notable exception of broad dispersive excitations within the vicinity of the 1D spin-orbit exciton. These broad excitations disperse towards higher energy as the momentum transfer approaches π (Figure 4.7b). Note that broad excitations in bulk Sr_2IrO_4 originate from the electron-hole continuum and damped orbital excitons. Thus, the broad dispersive excitations in the 1D IrO_2 stripe RIXS spectra are consistent with the

optical spectroscopy data (Figure 4.5b), which reveal the existence of a largely reduced electron-hole continuum. Hence, the observed broad orbital excitations reflect the
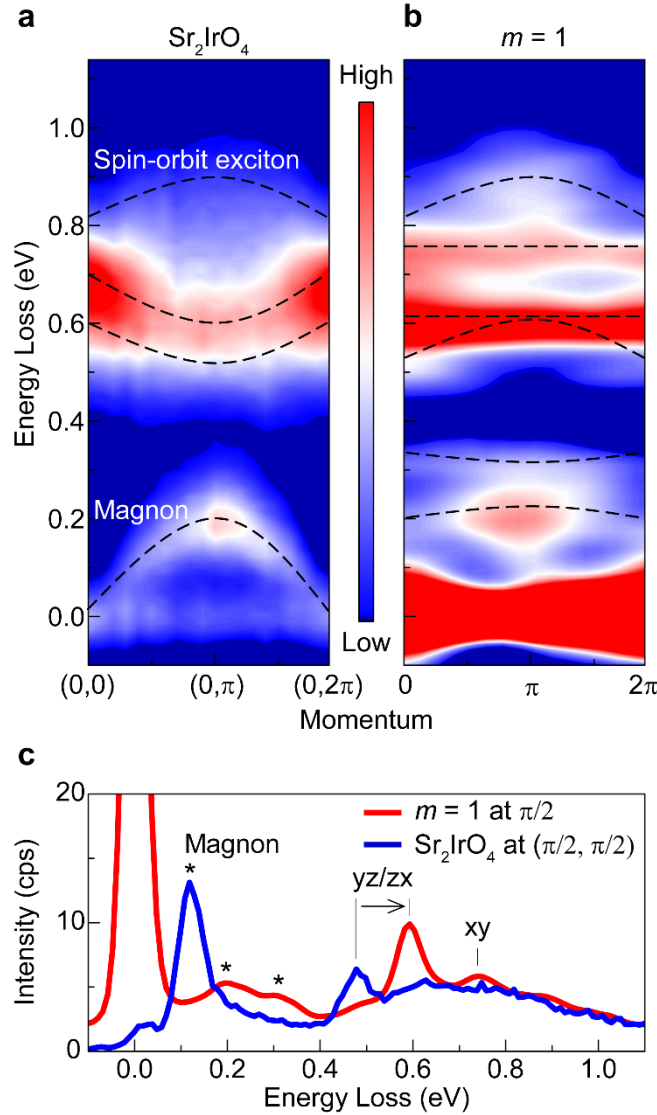
Figure 4.8: Intensity contour plots of RIXS spectra for a) 2D Sr_2IrO_4 crystal along the (0, 0) to (0, 2π) direction of its 2D Brillouin zone and b) 1D $(Sr_2IrO_4)_1/(LaSrGaO_4)_5$ superlattice along the 0 to 2π direction (i.e. parallel to the b-axis) of its 1D Brillouin zone. Note that the low-energy magnon branch and the dispersion of spin-orbit excitons are shown below 0.2 eV and above 0.4 eV, respectively, and dashed lines act as visual guides. c) RIXS spectra of the 1D superlattice (red) and 2D Sr_2IrO_4 crystal (blue) at comparable momentum transfers. Distinct excitations of the 1D superlattice include: broad spin-excitations below 0.4 eV are distinct from the resolution-limited magnon peak of 2D Sr_2IrO_4 (indiated by * in c)); the 1D superlattice shows a quasiparticle spin-orbit exciton at ca. 0.6 eV, of which energy is 100 meV higher than that of 2D Sr_2IrO_4; and broad orbital excitations also show different dispersive behaviors from 2D counterpart. The strong intensity around zero energy loss in b) is mostly from elastic scattering by $LaSrGaO_4$ layers.

46

deconfined character of orbitals in the 1D structure.

4.5   Density Functional Theory calculations of 1D dispersion

To supplement the understanding of the experimental data, we have performed density functional theory (DFT) calculations for the 1D $(Sr_2IrO_4)_1/(LaSrGaO_4)_5$ stripe-structure. As compared to its 2D Sr_2IrO_4 counterpart (Figure 4.8a), the spin-orbit split J_{eff} = 1/2 band appears quite flattened in the 1D energy dispersion (Figure 4.8b), indicating the
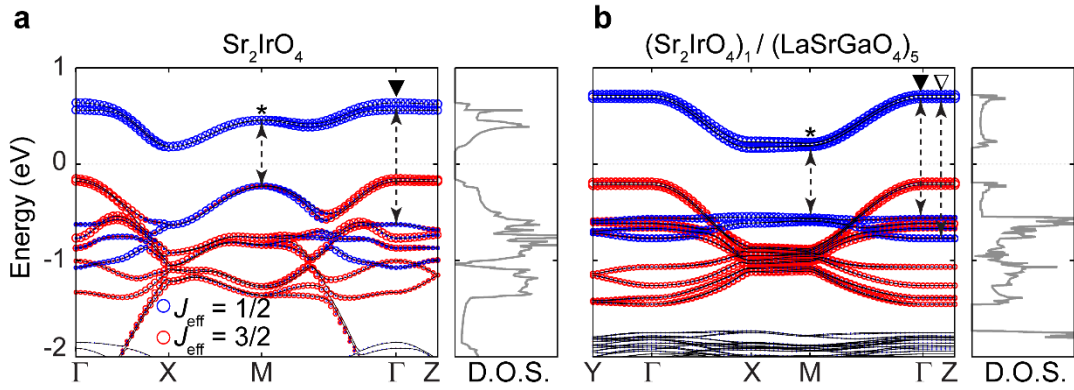
Figure 4.9: Band structures from DFT calculations and the density of states (DOS). a) The calculated electronic band structure (left) and DOS (right) of 2D Sr_2IrO_4. The J_{eff} = 1/2 and J_{eff} = 3/2 states are distinguished between blue and red circles, respectively. The optically allowed inter-band J_{eff} = 1/2 transitions are indicated by dashed lines, and the labels * and ▼ correspond to the observed peaks in the optical conductivity spectra in Figure 4.5b. b) The electronic band structure and DOS of 1D $(Sr_2IrO_4)_1/(LaSrGaO_4)_5$ superlattice show the flat dispersion due to dimensional confinement. An indirect-to-direct gap transition is consistent with experimental data (Figure 4.5c and Figure 4.5d). Sharp features (van Hove singularities) in the DOS and an additional optically allowed J_{eff} = 1/2 transition (∇) are in agreement with the experimental spectra in Figure 4.5b.

presence of a very localized J_{eff} = 1/2 state.

As a consequence, the indirect gap between the J_{eff} = 1/2 state in 2D Sr_2IrO_4 becomes a direct gap in its 1D counterpart, which is in excellent agreement with the indirect-to-direct gap phase transition observed in the optical spectra (Figure 4.5c and Figure 4.5d, respectively). The localization of the J_{eff} = 1/2 state should also induce

additional sharp optical transitions since optical spectroscopy measures the joint density of states between occupied and unoccupied bands. This result is consistent with the emergence of the van Hove singularity, i.e. sharp peak ∇, in the optical conductivity spectra of the superlattices (Figure 4.5b). The excellent agreement of these 1D characters with the experimentally obtained optical conductivity spectra verifies the successful electronic confinement of our $(Sr_2IrO_4)_m/(LaSrGaO_4)_5$ stripe-structures.

4.6   Outlook and Summary

This approach of creating 1D quantum-stripe systems provides an avenue for exploring emergent phenomena of low dimensional physics. For instance, superconducting 1D nano-stripes can be created by using an *a*-axis oriented superlattice of the layered cuprates such as $(La,Sr)_2CuO_4$. Although metallic ground states in true 1D materials are hard to stabilize due to structural instabilities such as the Peierls transition, the striped structures can be used to discover new phase transitions by tuning the system's dimensionality from two to one dimension(s).(81) Another intriguing feature of low dimensional systems is fractionalization of spin and charge degrees of freedom (e.g. spinons and excitons). Such excitonic effects are expected to be enhanced due to their spatial decoupling in 1D systems.

In summary, we have shown a generalizable superlattice approach of a continuous dimensional control between two-dimensional (2D) layered oxides and 1D quantum stripes. We demonstrated its successful application on the highly correlated, 2D Sr_2IrO_4. In our superlattice structures, we have observed the optical transitions of electrons between neighboring Ir atoms to be confined to the 1D IrO_2 stripe direction, which emulates ideal 1D behavior. Spin and orbital excitations observed in resonant inelastic x-ray scattering

also suggest enhanced spin exchange interactions and confined orbital excitations in the 1D IrO_2 stripes as compared to 2D Sr_2IrO_4. This 1D superlattice method can be readily adopted for unveiling 1D phenomena in a variety of two-dimensional materials.

Pyrochlore iridates ($R_2Ir_2O_7$, R: rare-earth lanthanides) have attracted substantial attention

for predictions of topological properties emerging from frustrated magnetic spin structures

(all in – all out AIAO ordering) in the presence of strong spin-orbit interaction and effective

electron correlation U_{eff} (2,82). The lattice structure of the pyrochlore iridates consists of

two interwoven kagome sublattices—a tetrahedral network formed by Ir-O and a corner

shared tetrahedral network formed by the rare-earth atoms (see Figure 5.1). The $J_{eff} = \frac{1}{2}$
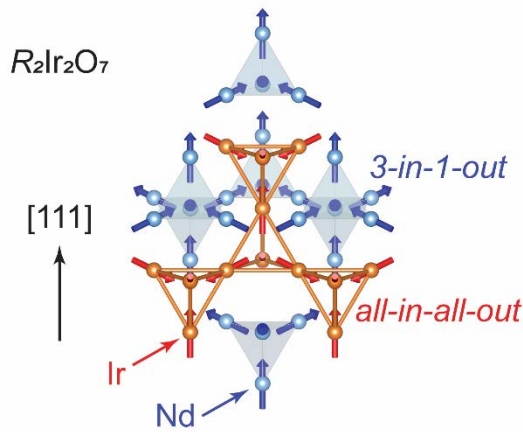
Figure 5.1: Pyrochlore iridate $R_2Ir_2O_7$ lattice structure. The pyrochlore lattice features two interwoven kagome sublattices of corner sharing tetrahedra. The Ir (orange) atoms form tetrahedra via an Ir-O network (oxygen not depicted) and are pictured in the geometrically frustrated all-in-all-out spin configuration. The R (blue) atoms are rare-earth atoms of the lanthanide series and form tetrahedra around an oxygen atom (not pictured). The R-sublattice is pictured in the 3-in-1-out spin configuration.

spins of the Ir sublattice point either inward or outward towards the center of each

tetrahedra. These all-in-all-out (AIAO) and all-out-all-in (AOAI) magnetic orderings are

degenerate ground states (hence frustrated) and form a unique octupole antiferromagnetic

order (83). Experimental evidence suggests this magnetic order is concomitant with a

metal-insulator transition in several pyrochlore iridate systems (84-86).

The spin-orbit-split $J_{eff} = 1/2$ state arranged on a kagome lattice has been theoretically shown to take a paramagnetic semimetallic ground state when $U_{eff} = 0$ (2). However, as U_{eff} is turned on to a small finite value, it stabilities the AIAO spin configuration and induces a Weyl semimetal state with 8 Weyl points along the [111] and symmetry related directions. As U_{eff} is increased further, each Weyl point pair moves in momentum space along its respective symmetry direction until the points pair-annihilate at the Brillouin zone boundary. At this point, the system's bulk bands become insulating while the surface states remain conducting. These surface states remain conducting until a further increase in U_{eff} gaps the surface state, and thus the system forms a Mott insulating state. Figure 5.2, recreated from Ref. (2), summaries the phase dynamics of this system.
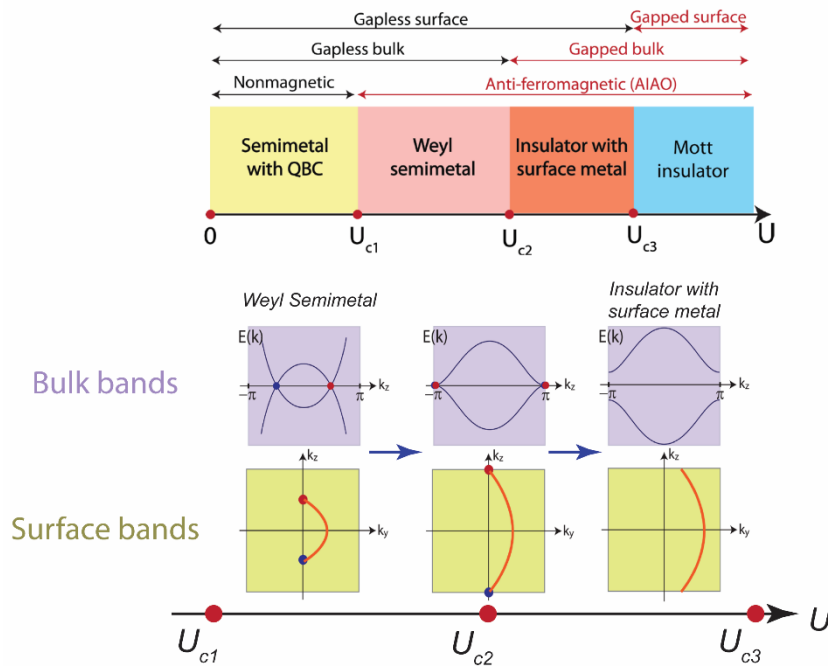
Figure 5.2: Pyrochlore iridate electronic and magnetic phase diagram as a function of U. The top panel describes the evolution of the pyrochlore iridate system from a paramagnetic metal at $U=0$ through the AIAO Weyl semi metallic phase, until reaching the Mott insulating phase. The bottom panel depicts a Weyl point pair (blue and red dots) in the bulk and surface bands. The pair annihilates at U_{c2}, and opens a bulk gap. This figure has been recreated from Ref. (2).

5.1   Motivation of study

A method for probing this multi-interaction phase space is by monotonically tuning U_{eff}, which is achieved experimentally by altering the pyrochlore iridate lattice size, i. e. U_{eff} increases as the size of R decreases. This has been performed on a number of bulk polycrystalline samples with mixed concentrations of the lanthanide series rare-earths R, and the metal-insulator transition temperature T_{MI} has been observed to decrease as the rare-earth ionic radius size increases from Y to Pr – consistent with tuning U_{eff} (4,87). Recently, evidence for a field-induced transition between a Weyl semimetal to a line node semimetal has also been reported in bulk single crystals of $Nd_2Ir_2O_7$ and $(Pr_{1/2}Nd_{1/2})_2Ir_2O_7$ (88). This encouraging find supports further investigation into the topological properties of other pyrochlore iridate members with various values of U_{eff} to determine the critical phase boundaries between the distinct surface and bulk ground states.

5.2   Synthesis of mixed-phase $(A,B)_2Ir_2O_7$ thin-films

In order to tune U_{eff} in this study, we have synthesized a series of mixed phase pyrochlore iridate thin-films $((A,B)_2Ir_2O_7$ for (A,B) = $(Pr_{1/2}Nd_{1/2})$; $(Pr_{1/3}Nd_{2/3})$; (Nd); $(Sm_{1/3}Nd_{2/3})$; $(Sm_{1/2}Nd_{1/2})$; $(Sm_{2/3}Nd_{1/3})$; (Sm)) on the wide-band insulator $Y:ZrO_2$ (YSZ) using a combination of pulsed laser deposition and a high-temperature anneal in ambient, which has been reported elsewhere (89). As the average rare earth ionic size is increased from Sm to $Pr_{1/2}Nd_{1/2}$, the thin-film lattice parameters systematically increase, as revealed by x-ray diffraction 2θ scans and reciprocal space maps (Figure 5.3abd). While the lattice size increase is consistent with those of bulk polycrystals (4), the films have rather broad RSM reflection peaks, indicating substantial film relaxation. Although relaxed, the Raman
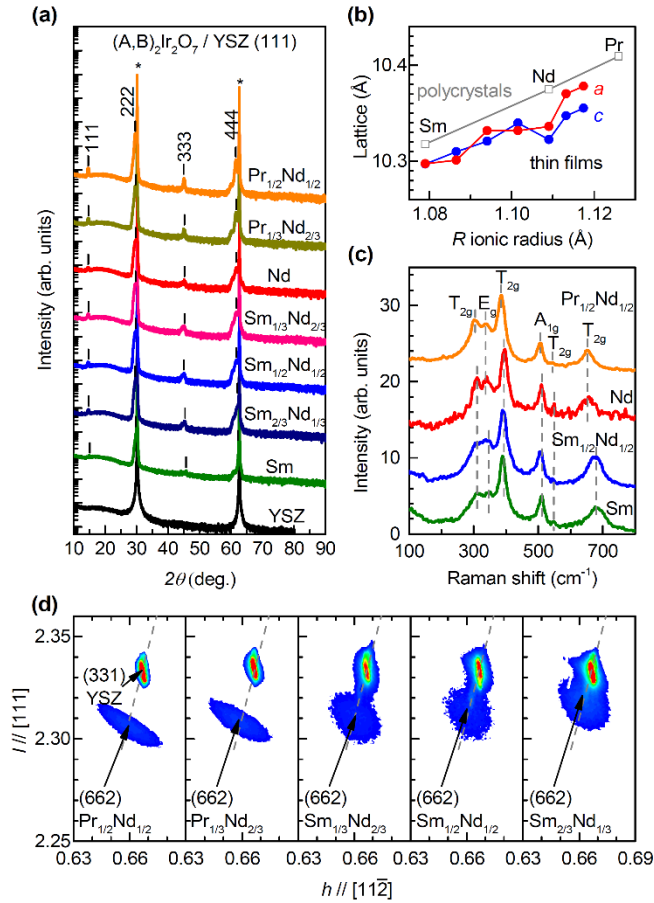
Figure 5.3: X-ray diffraction and Raman spectra of mixed phase pyrochlore iridates $(A,B)_2$ Ir_2O_7 / YSZ (111). (a) Symmetric x-ray diffraction scans for the mixed-rare earth series (A,B) including $(Pr_{1/2}Nd_{1/2})$; $(Pr_{1/3}Nd_{2/3})$; (Nd); $(Sm_{1/3}Nd_{2/3})$; $(Sm_{1/2}Nd_{1/2})$; $(Sm_{2/3}Nd_{1/3})$; (Sm), where the average rare-earth ionic radius is sequentially decreased. All samples take the pyrochlore structure with the (111)-lattice vector parallel to the out-of-plane direction. The dashed lines are placed at the out-of-plane diffraction peaks for single-phase $Nd_2Ir_2O_7$ (b) The out-of-plane lattice constants for the mixed-phase films calculated from each film's reciprocal space map diffraction peak. As the average rare-earth ionic radius size is increased from (Sm) to $(Pr_{1/2}Nd_{1/2})$, the pyrochlore iridate lattice parameters sequentially increase and are consistent with polycrystalline, single-phase samples reported by Ref. (4). (c) Raman spectra taken at room temperature indicate the presence of the six phonon modes expected of the pyrochlore structure (d) RSM's of each film's (662)-reflection peak. The dashed gray curve represents the line of cubic lattice constants, which are expected for the pyrochlore structure.

spectra indicate the films have the six Raman active phonon modes consistent with the

pyrochlore lattice symmetry (Figure 5.3c) (90). Additionally, temperature dependent

resistivity shows the films to all undergo a metal-insulator transition (Figure 5.4), which is
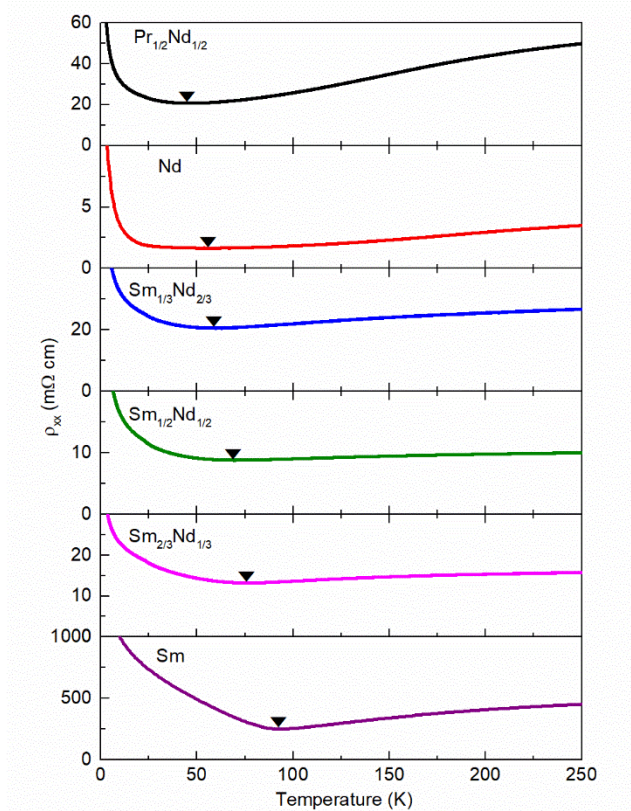
Figure 5.4: Resistivity measurements of the mixed-phase pyrochlore iridates in zero applied field. The black triangle represents the metal-insulator transition temperature of each mixed-phase film and systematically increases as the rare-earth ionic radius size decreases (ordered from top to bottom).

consistent with the expectation that tuning the ionic radius from Sm to $Pr_{1/2}Nd_{1/2}$ will systematically decrease U_{eff}.

5.3   Comparison with bulk single crystal pyrochlore iridates

Comparing the residual resistivity ratio (RRR) of the thin film samples with that of bulk single crystal $Nd_2Ir_2O_7$ (3), the thin film samples have RRR values several orders of magnitude lower than that of the bulk samples (Figure 5.5). Additionally, the thin films have a much broader MIT transition than the sharp transition of bulk $Nd_2Ir_2O_7$. This comparison indicates the pyrochlore iridate thin films have a higher degree of disorder than
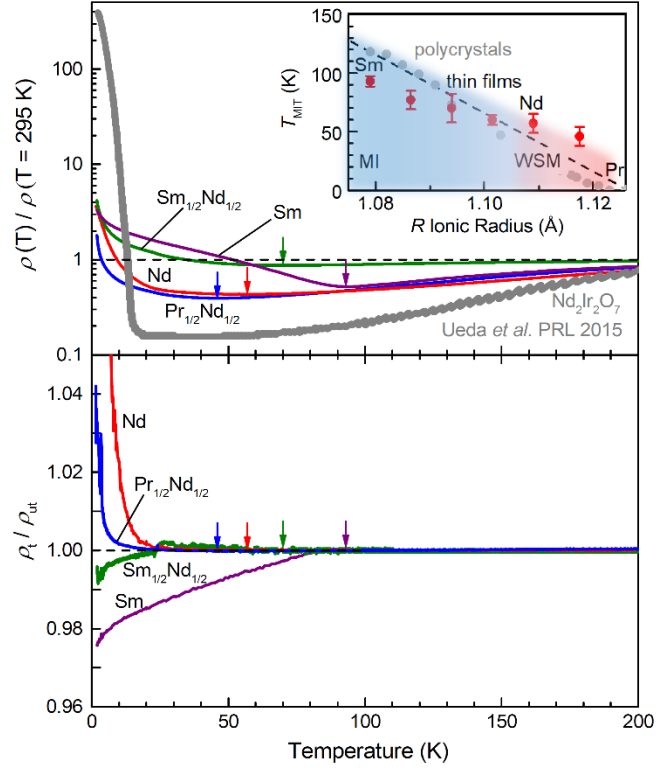
Figure 5.5: Residual resistivity ratio comparison between mixed-phase pyrochlore films and bulk single crystal $Nd_2Ir_2O_7$ (upper panel). While the mixed-phase pyrochlore films each undergo a metal-insulator transition that is consistent with the tuning of U_{eff}, the transition is rather broad compared to the sharp transition observed in bulk single crystal $Nd_2Ir_2O_7$ (recreated from Ref. (3)). The residual resistivity ratios of the thin-film samples are also two orders of magnitude less than that of the bulk single crystal. The bottom panel displays the surface state conduction property of each mixed phase pyrochlore film by taking the resistivity ratio between films trained in a 14 T field and their untrained resistivity. As U_{eff} increases from $Pr_{1/2}Nd_{1/2}$ to Sm, the surface conduction becomes insulating. The inset in the top panel is a phase diagram reconciling the topological properties of Figure 5.2 with the domain wall and bulk conducting properties. The light gray dots are polycrystalline bulk samples reported in Ref. (4).

the bulk single crystals reported in previous studies. While the thin films may be of inferior quality to that of bulk single crystals, this feature can be used as an important tool for investigating the topologically protected ground states expected in these pyrochlore systems. Because the conducting mechanisms of topologically non-trivial systems are protected by symmetry, they should be robust against crystalline defeats and disorder, which is difficult to access in high-quality, bulk single crystals (91). Therefore, these more

disordered mixed-phase films can offer strong supporting evidence for the robust nature of the topological properties in the pyrochlore iridate system.

In order to reconcile the mixed-phase pyrochlore thin films with the phase diagram in Figure 5.2, it is necessary to access the surface state conduction properties, which are manifest on the magnetic domain walls (84). To isolate the surface state conduction from the bulk conduction properties, the films are cooled under an applied field of 14 T (trained) and the resultant warming resistivity ρ_{trained} under zero-field is then compared to the untrained resistivity $\rho_{\text{untrained}}$ (Figure 5.5). If surface conduction is present (absent), the resistivity ratio between trained and untrained films will be greater than (equal to or less than) one, since the cooling under an applied field stabilizes a single domain configuration. For the thin-films, a systematic change in the domain wall conducting behavior from insulating to metallic domain walls is observed as the A-site radius is increased from Sm to $Pr_{1/2}Nd_{1/2}$, which is consistent with the change in U_{eff} across the Mott insulating to Weyl semimetal phases. Combining the surface state conduction property with each film's metal-insulator transition temperature, a phase diagram can be assigned for each mixed-phase pyrochlore thin film (Figure 5.5).
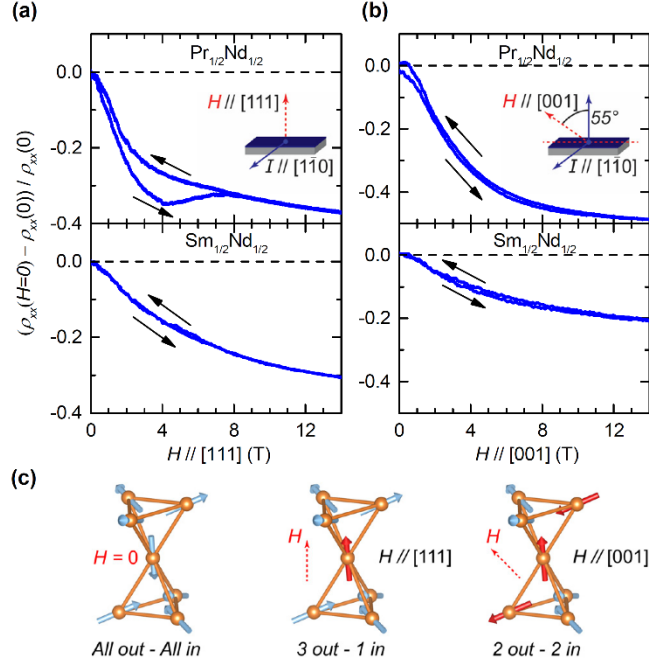
Figure 5.6: Magneto-transport of the mixed phase pyrochlore iridate thin films at 2 K. The magneto-resistance is taken of the mixed phase pyrochlore films for $R = Pr_{1/2}Nd_{1/2}$ and $Sm_{1/2}Nd_{1/2}$, i. e. comparing the response of a Weyl semimetal with that of a Mott insulator, respectively. The field sweeps are taken such that the applied field is oriented parallel to each film's (a) [111] and (b) [001] crystallographic directions (see inset diagrams). (c) Schematic spin configurations showing, from left to right, the all out – all in, 3 out – 1 in, and 2 out – 2 in magnetic order induced when $H = 0$, $H \mathbin{/\mkern-4mu/} [111]$, and $H \mathbin{/\mkern-4mu/} [001]$, respectively.

To investigate this further, we accessed the magnetic ordering of the films using field sweeps at 2 K, i. e. below the magnetic ordering temperature (Figure 5.6). It is understood from previous studies on $Nd_2Ir_2O_7$ that a strong applied field parallel to the [111] ([001]) crystallographic axis flips the all-in-all-out spin ordering of the Ir-sublattice into a 3 out – 1 in (2 out – 2 in) spin configuration (Figure 5.6ab) (88). The distinction is clear in the presence (absence) of hysteretic behavior when the field is parallel to the [111] ([001]) direction. For the thin films, distinct hysteretic behaviors are apparent for $Pr_{1/2}Nd_{1/2}$ when $H \mathbin{/\mkern-4mu/} [111]$, marking a spin flip into a 3 out – 1 in configuration (Figure 5.6c). This is consistent with the 3/1 Weyl semimetal phase observed in the $Nd_2Ir_2O_7$ bulk case (88). When $H \mathbin{/\mkern-4mu/} [001]$, the applied field can flip two spins to form 2 out – 2 in spin ordering

(Figure 5.6c). This is supported by the vanishing hysteretic behavior and implies a field-induced electronic reconstruction has occurred. For the $Sm_{1/2}Nd_{1/2}$ thin films, the magneto-resistance behavior appears independent of field direction. This is consistent with the larger U_{eff} present in these compounds, which acts to stabilize the zero-field spin configuration. Although the field sweeps offer important evidence for the distinct electronic ground states between $Pr_{1/2}Nd_{1/2}$ and $Sm_{1/2}Nd_{1/2}$, it is difficult to gain deeper insight from the field sweeps displaying non-hysteretic behavior.

5.4   Rotational dependent magneto-transport

Rotational dependent magneto-transport can generate field-induced changes in the spin structures, which are accompanied with drastic changes in conductivity due to a reconfiguration of the underlying electronic structure. For instance, in bulk single crystal $Nd_2Ir_2O_7$, spin flips to the 2 out – 2 in spin structure generate a very large, smooth increase in the magneto-conductance while spin flips between 3 out – 1 in and 1 out – 3 in configurations generate conduction spikes during the transition (3). For the 2 out – 2 in transition, the observed increase in bulk conductivity is consistent with a topological reconstruction to a line node semi-metal (88). For transitions between the 3 out – 1 in state and its time-reversal pair, the topological texture remains unchanged. However, the conduction spikes observed during the transition are a result of the propagation of conducting domain walls, which are consistent with the conducting surface states expected of a Weyl semi-metal phase (3). Here we have measured rotational dependent field conductivity for $Pr_{1/2}Nd_{1/2}$ and $Sm_{1/2}Nd_{1/2}$ of the mixed phase thin films (Figure 5.7). The $Pr_{1/2}Nd_{1/2}$ sample's rotational field dependence is very similar to that of bulk single crystal $Nd_2Ir_2O_7$. Namely, the spikes in conductivity are the result of a field induced spin flip from

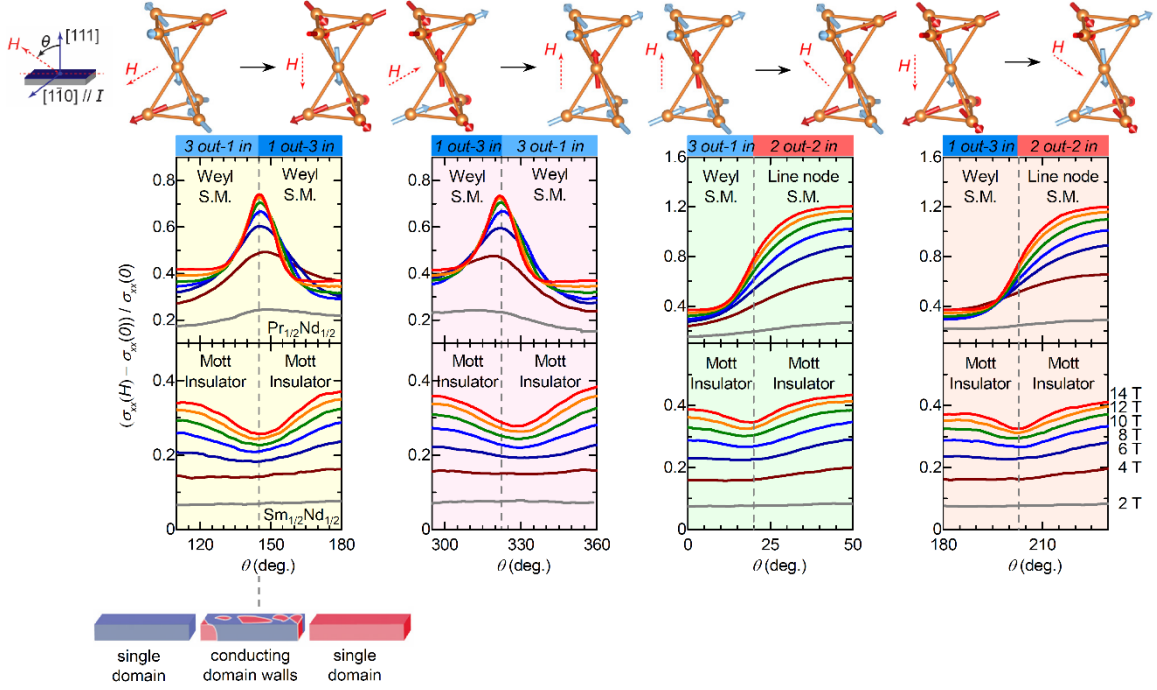Figure 5.7: Rotational dependent magneto-transport of $Pr_{1/2}Nd_{1/2}Ir_2O_7$ (top row) and $Sm_{1/2}Nd_{1/2}Ir_2O_7$ (bottom row) thin films at 2K. The current is directed along the $[1\bar{1}0]$ direction and is parallel to the axis of rotation, i. e. perpendicular to H (depicted in top left diagram). The fixed field is then rotated through a complete $360°$ rotation. The two leftmost panels display the conducting spikes (dips) observed in $Pr_{1/2}Nd_{1/2}Ir_2O_7$ ($Sm_{1/2}Nd_{1/2}Ir_2O_7$) when the spin state changes between 3 out – 1 in and 1 out – 3 in. When switching between these states, a propagation of conducting (insulating) domain walls induces the spike (dip) in conductivity during the transition, as depicted in the schematic under the first panel. The two rightmost panels depict spin flips from 3 out – 1 in (1 out – 3 in) to 2 out – 2 in. For $Pr_{1/2}Nd_{1/2}$, the smooth increase in magneto-conductance is consistent with a transition to a line node semi-metal (S. M.). For $Sm_{1/2}Nd_{1/2}$, the Mott insulating state is retained during the spin-flip transition.

3 out – 1 in to 1 out – 3 in configurations (Figure 5.7) and are consistent with the Weyl semimetal property of bulk $Nd_2Ir_2O_7$. However, the large gradual increase in conductivity observed during the spin flip to the 2 out – 2 in configuration (Figure 5.7) is consistent with an electronic rearrangement of a line node semimetal. These transitions are observed for both time-reversal pair field directions.

The $Sm_{1/2}Nd_{1/2}$, which has a greater U_{eff}, has a distinct electronic configuration from that of the $Pr_{1/2}Nd_{1/2}$ sample. The $Sm_{1/2}Nd_{1/2}$ remains in an insulating Mott state and spin transitions are marked by dips in conductivity, rather than spikes (Figure 5.7). Since this

compound has a larger U_{eff}, it retains its insulating nature during the field-induced spin flips. This is consistent with the theoretical phase diagram in Figure 5.2, where a large U_{eff} opens a gap in both the surface and bulk states.

5.5   Conclusions

The mixed-phase pyrochlore iridate thin-films offer an effective means for tuning U_{eff} across distinct electronic phase boundaries. While the quality of the mixed phase thin-films is inferior to that of bulk single crystals, the films still emanate field-induced topological properties consistent with that reported in high-quality bulk single crystals. Additionally, the large U_{eff} in $Sm_{1/2}Nd_{1/2}Ir_2O_7$ thin films is too large for the formation of the Weyl points, and hence takes a Mott insulating state—indicating a clear distinction from the Weyl semimetallic spin character observed in $Pr_{1/2}Nd_{1/2}Ir_2O_7$. This study provides evidence for the robust nature of a Weyl semimetal, while also demonstrating the strong dependence of U_{eff} in stabilizing this ground state.

Appendix

Fresnel reflection coefficients for isotropic single slab model

For an isotropic, smooth layer (1) on an isotropic substrate (2) in an isotropic ambient (0), the complex Fresnel reflection coefficients are

$$\tilde{R}_p = \frac{r_{01p} + r_{12p} \exp[-i2\beta]}{1 + r_{01p}r_{12p} \exp[-i2\beta]} \tag{A. 1}$$

$$\tilde{R}_s = \frac{r_{01s} + r_{12s} \exp[-i2\beta]}{1 + r_{01s}r_{12s} \exp[-i2\beta]}, \tag{A. 2}$$

Where r_{01p}, r_{12p}, and r_{01s}, r_{12s} are the reflection coefficients at the 0-1 ambient-film and 1-2 film-substrate interfaces for *p*- and *s*- polarization states. Using appropriate boundary matching conditions from Maxwell's equations and application of Snell's law, these reflection coefficients can be found

$$r_{01p} = \frac{N_1^2 \cos \varphi_0 - N_0 N_1 \cos \varphi_1}{N_1^2 \cos \varphi_0 + N_0 N_1 \cos \varphi_1} \tag{A. 3}$$

$$r_{12p} = \frac{-N_1^2 \cos \varphi_2 + N_2 N_1 \cos \varphi_1}{N_1^2 \cos \varphi_0 + N_2 N_1 \cos \varphi_1} \tag{A. 4}$$

$$r_{01s} = \frac{N_0 \cos \varphi_0 - N_1 \cos \varphi_1}{N_0 \cos \varphi_0 + N_1 \cos \varphi_1} \tag{A. 5}$$

$$r_{12s} = \frac{-N_2 \cos \varphi_2 + N_1 \cos \varphi_1}{N_2 \cos \varphi_2 + N_1 \cos \varphi_1}, \tag{A. 6}$$

where N_0, N_1, and N_2 are the complex refractive indices of each respective layer ($N_j = n_j + ik_j$), φ_0 is the angle of incidence, and φ_1, φ_2 are the angles of refraction for the film and substrate, respectively.

β is the phase change associated with light's propagation through the thin-film of thickness d and is given for an isotropic film by

$$\beta = 2\pi \left(\frac{d}{\lambda}\right) (N_1^2 - N_0^2 \sin \varphi_0)^{1/2}. \tag{A. 7}$$

Substituting Equations (A. 3)-(A. 7) into Equations (A. 1) and (A. 2), the complex Fresnel reflection coefficients can be related to the ellipsometric data (Ψ and Δ) by Equation (2.3).

References

[1]   M. Imada, A. Fujimori, and Y. Tokura, Reviews of Modern Physics **70**, 1039 (1998).

[2]   S. Robert, L. Eric Kin-Ho, Y. Bohm-Jung, and K. Yong Baek, Reports on Progress in Physics **79**, 094504 (2016).

[3]   K. Ueda, J. Fujioka, B. J. Yang, J. Shiogai, A. Tsukazaki, S. Nakamura, S. Awaji, N. Nagaosa, and Y. Tokura, Physical Review Letters **115**, 056402 (2015).

[4]   K. Ueda, J. Fujioka, C. Terakura, and Y. Tokura, Physical Review B **92**, 121110 (2015).

[5]   H. Kamerlingh Onnes, Comm. Phys. Lab. Univ. Leiden **122b** (1911).

[6]   J. Bardeen, L. N. Cooper, and J. R. Schrieffer, Physical Review **106**, 162 (1957).

[7]   L. R. Testardi, J. H. Wernick, and W. A. Royer, Solid State Communications **15**, 1 (1974).

[8]   C. Kittel, *Introduction to Solid State Physics* (Wiley, 1996).

[9]   J. G. Bednorz and K. A. Muller, Zeitschrift fur Physik B Condensed Matter **64**, 189 (1986).

[10]   M. K. Wu, J. R. Ashburn, C. J. Torng, P. H. Hor, R. L. Meng, L. Gao, Z. J. Huang, Y. Q. Wang, and C. W. Chu, Physical Review Letters **58**, 908 (1987).

[11]   M. M. Waldrop, Science **238**, 481 (1987).

[12]   L. H. Thomas, Nature **117**, 514 (1926).

[13]   R. Shankar, *Principles of Quantum Mechanics* (Plenum Press, New York, 1994), 2nd edn.

[14]   J. H. d. Boer and E. J. W. Verwey, Proceedings of the Physical Society **49**, 59 (1937).

[15] J. Hubbard, Proceedings of the Royal Society of London. Series A. Mathematical and Physical Sciences **276**, 238 (1963).

[16] J. S. Horwitz *et al.*, Applied Surface Science **127**, 507 (1998).

[17] D. H. Lowndes, D. B. Geohegan, A. A. Puretzky, D. P. Norton, and C. M. Rouleau, Science **273**, 898 (1996).

[18] J. Mannhart and D. G. Schlom, Science **327**, 1607 (2010).

[19] D. Dijkkamp, T. Venkatesan, X. D. Wu, S. A. Shaheen, N. Jisrawi, Y. H. Minlee, W. L. McLean, and M. Croft, Applied Physics Letters **51**, 619 (1987).

[20] H. W. Jang *et al.*, Physical Review Letters **104**, 197601 (2010).

[21] D. B. Chrisey and G. K. Hubler, *Pulsed Laser Deposition of Thin Films* (Wiley, New York, 1994).

[22] J. Shen, Z. Gai, and J. Kirschner, Surface Science Reports **52**, 163 (2004).

[23] H. N. Lee, H. M. Christen, M. F. Chisholm, C. M. Rouleau, and D. H. Lowndes, Nature **433**, 395 (2005).

[24] G. J. H. M. Rijnders, G. Koster, D. H. A. Blank, and H. Rogalla, Materials Science and Engineering: B **56**, 223 (1998).

[25] T. Maeda, G. H. Lee, T. Ohnishi, M. Kawasaki, M. Yoshimoto, and H. Koinuma, Materials Science and Engineering: B **41**, 134 (1996).

[26] H. Karl and B. Stritzker, Physical Review Letters **69**, 2939 (1992).

[27] T. Terashima, Y. Bando, K. Iijima, K. Yamamoto, K. Hirata, K. Hayashi, K. Kamigaki, and H. Terauchi, Physical Review Letters **65**, 2684 (1990).

[28] G. J. H. M. Rijnders, G. Koster, D. H. A. Blank, and H. Rogalla, Applied Physics Letters **70**, 1888 (1997).

[29]   D. H. A. Blank and H. Rogalla, MRS Proceedings **502**, 237 (2011).

[30]   M. E. Bijlsma, D. H. A. Blank, H. Wormeester, A. van Silfhout, and H. Rogalla, Journal of Alloys and Compounds **251**, 15 (1997).

[31]   M. E. Bijlsma, H. Wormeester, D. H. A. Blank, E. Span, A. v. Silfhout, and H. Rogalla, Physical Review B **57**, 13418 (1998).

[32]   J. Lekner, J. Opt. Soc. Am. A **14**, 1355 (1997).

[33]   D. U. Fluckiger, J. Opt. Soc. Am. A **15**, 2228 (1998).

[34]   J. G. Connell, B. J. Isaac, G. B. Ekanayake, D. R. Strachan, and S. S. A. Seo, Applied Physics Letters **101**, 251607 (2012).

[35]   T. Frey, C. C. Chi, C. C. Tsuei, T. Shaw, and F. Bozso, Physical Review B **49**, 3483 (1994).

[36]   N. Grandjean, J. Massies, M. Leroux, J. Leymarie, A. Vasson, and A. M. Vasson, Applied Physics Letters **64**, 2664 (1994).

[37]   R. M. A. Azzam and N. M. Bashara, *Ellipsometry and polarized light* (North-Holland Pub. Co. ; Elsevier North-Holland, Amsterdam ; New York : New York, 1977), Accessed from http://nla.gov.au/nla.cat-vn2207147.

[38]   W. S. Choi, D. W. Jeong, S. S. A. Seo, Y. S. Lee, T. H. Kim, S. Y. Jang, H. N. Lee, and K. Myung-Whun, Physical Review B **83**, 195113 (2011).

[39]   P. Lautenschlager, M. Garriga, L. Vina, and M. Cardona, Physical Review B **36**, 4821 (1987).

[40]   K. Kamaras *et al.*, Physical Review Letters **59**, 919 (1987).

[41]   S. Moon *et al.*, Physical Review Letters **101** (2008).

[42]   C. Rayan Serrao *et al.*, Physical Review B **87**, 085121 (2013).

[43]   J. Nichols, J. Terzic, E. G. Bittle, O. B. Korneta, L. E. De Long, J. W. Brill, G. Cao, and S. S. A. Seo, Applied Physics Letters **102**, 141908 (2013).

[44]   N. Mott, in *The Physics of Hydrogenated Amorphous Silicon II*, edited by J. Joannopoulos, and G. Lucovsky (Springer Berlin Heidelberg, 1984), pp. 169.

[45]   J. M. Longo, J. A. Kafalas, and R. J. Arnott, Journal of Solid State Chemistry **3**, 174 (1971).

[46]   J. G. Zhao, L. X. Yang, Y. Yu, F. Y. Li, R. C. Yu, Z. Fang, L. C. Chen, and C. Q. Jin, Journal of Applied Physics **103**, 103706 (2008).

[47]   K. Yong Kwan *et al.*, Japanese Journal of Applied Physics **45**, L36 (2006).

[48]   S. Y. Jang, S. J. Moon, B. C. Jeon, and J. S. Chung, J Korean Phys Soc **56**, 1814 (2010).

[49]   A. Biswas, K.-S. Kim, and Y. H. Jeong, arXiv, 1312.2716 (2013).

[50]   S. Y. Jang, H. Kim, S. J. Moon, W. S. Choi, B. C. Jeon, J. Yu, and T. W. Noh, Journal of physics. Condensed matter : an Institute of Physics journal **22**, 485602 (2010).

[51]   J. Liu *et al.*, ArXiv, 1305.1732 (2013).

[52]   N. Gayathri, A. K. Raychaudhuri, X. Q. Xu, J. L. Peng, and R. L. Greene, Journal of Physics: Condensed Matter **10**, 1323 (1998).

[53]   F. X. Wu, J. Zhou, L. Y. Zhang, Y. B. Chen, S. T. Zhang, Z. B. Gu, S. H. Yao, and Y. F. Chen, Journal of physics. Condensed matter : an Institute of Physics journal **25**, 125604 (2013).

[54]   G. Bergmann, Physics Reports **107**, 1 (1984).

[55]   J. M. Luttinger, Journal of Mathematical Physics **4**, 1154 (1963).

[56]   S. Dong, R. Yu, J. M. Liu, and E. Dagotto, Physical Review Letters **103**, 107204 (2009).

[57]   H. A. Mook, P. C. Dai, F. Dogan, and R. D. Hunt, Nature **404**, 729 (2000).

[58]   S. A. Kivelson, I. P. Bindloss, E. Fradkin, V. Oganesyan, J. M. Tranquada, A. Kapitulnik, and C. Howald, Reviews of Modern Physics **75**, 1201 (2003).

[59]   D. N. Sheng, Z. Y. Weng, L. Sheng, and F. D. M. Haldane, Physical Review Letters **97**, 036808 (2006).

[60]   L. Fu, C. L. Kane, and E. J. Mele, Physical Review Letters **98**, 106803 (2007).

[61]   D. Hsieh, D. Qian, L. Wray, Y. Xia, Y. S. Hor, R. J. Cava, and M. Z. Hasan, Nature **452**, 970 (2008).

[62]   Y. L. Chen *et al.*, Science **325**, 178 (2009).

[63]   Y. N. Xia, P. D. Yang, Y. G. Sun, Y. Y. Wu, B. Mayers, B. Gates, Y. D. Yin, F. Kim, and Y. Q. Yan, Adv Mater **15**, 353 (2003).

[64]   C. Kim, A. Y. Matsuura, Z. X. Shen, N. Motoyama, H. Eisaki, S. Uchida, T. Tohyama, and S. Maekawa, Physical Review Letters **77**, 4054 (1996).

[65]   E. Dagotto and T. M. Rice, Science **271**, 618 (1996).

[66]   J. Nichols, O. B. Korneta, J. Terzic, L. E. De Long, G. Cao, J. W. Brill, and S. S. A. Seo, Applied Physics Letters **103**, 131910 (2013).

[67]   S. Madhavan, D. G. Schlom, A. Dabkowski, H. A. Dabkowska, and Y. Liu, Applied Physics Letters **68**, 559 (1996).

[68]   J. Matsuno, Y. Okimoto, M. Kawasaki, and Y. Tokura, Physical Review Letters **95**, 176404 (2005).

[69]   J. H. Gruenewald, J. Nichols, and S. S. A. Seo, Rev Sci Instrum **84**, 043902 (2013).

[70]   B. J. Kim *et al.*, Physical Review Letters **101**, 076402 (2008).

[71] B. J. Kim, H. Ohsumi, T. Komesu, S. Sakai, T. Morita, H. Takagi, and T. Arima, Science **323**, 1329 (2009).

[72] S. J. Moon *et al.*, Physical Review Letters **101**, 226402 (2008).

[73] J. H. Gruenewald, J. Nichols, J. Terzic, G. Cao, J. W. Brill, and S. S. A. Seo, J Mater Res **29**, 2491 (2014).

[74] J. Kim, M. Daghofer, A. H. Said, T. Gog, J. van den Brink, G. Khaliullin, and B. J. Kim, Nature Communications **5**, 4453 (2014).

[75] B. H. Kim, G. Khaliullin, and B. I. Min, Physical Review Letters **109**, 167205 (2012).

[76] Y. K. Kim, N. H. Sung, J. D. Denlinger, and B. J. Kim, Nature Physics **12**, 37 (2016).

[77] F. Wang and T. Senthil, Physical Review Letters **106**, 136402 (2011).

[78] S. J. Moon, H. Jin, W. S. Choi, J. S. Lee, S. S. A. Seo, J. Yu, G. Cao, T. W. Noh, and Y. S. Lee, Physical Review B **80**, 195110 (2009).

[79] C. H. Sohn *et al.*, Physical Review B **90**, 041105 (2014).

[80] L. Van Hove, Physical Review **89**, 1189 (1953).

[81] E. R. Gagliano, C. R. Proetto, and C. A. Balseiro, Physical Review B **36**, 2257 (1987).

[82] W. Witczak-Krempa, G. Chen, Y. B. Kim, and L. Balents, Annual Review of Condensed Matter Physics **5**, 57 (2014).

[83] T.-h. Arima, Journal of the Physical Society of Japan **82**, 013705 (2012).

[84] E. Y. Ma *et al.*, Science **350**, 538 (2015).

[85] J. P. Clancy *et al.*, Physical Review B **94**, 024408 (2016).

[86]   C. Donnerer *et al.*, Physical Review Letters **117**, 037201 (2016).

[87]   K. Ueda, J. Fujioka, and Y. Tokura, Physical Review B **93**, 245120 (2016).

[88]   K. Ueda, T. Oh, B.-J. Yang, R. Kaneko, J. Fujioka, N. Nagaosa, and Y. Tokura, **8**, 15515 (2017).

[89]   T. C. Fujita, Y. Kozuka, M. Uchida, A. Tsukazaki, T. Arima, and M. Kawasaki, Scientific Reports **5**, 9711 (2015).

[90]   H. C. Gupta, S. Brown, N. Rani, and V. B. Gohel, Journal of Raman Spectroscopy **32**, 41 (2001).

[91]   J. E. Moore, Nature **464**, 194 (2010).

Vita

John Henry Gruenewald

Place of birth

St. Louis, Missouri

Educational Background

UNIVERSITY OF KENTUCKY,
Lexington, KY
Ph. D. in Condensed Matter Physics, December 2017 (expected)

UNIVERSITY OF KENTUCKY,
Lexington, KY
M. S. in Physics, April 2013

CENTRE COLLEGE,
Danville, KY
B. S. in Physics and Mathematics, May 2010

Professional Positions

Researcher at Institute for Basic Science – Center for Correlated Electron Systems,
Seoul National University, April 2016 – March 2017

Research Assistant for Dr. Ambrose Seo,
University of Kentucky, June 2012 – August 2017

Teaching Assistant for Physics & Astronomy Department,
University of Kentucky, August 2011 – May 2012

Publications

1. M. Souri, B. H. Kim, <u>J. H. Gruenewald</u>, J. G. Connell, J. Thompson, J. Nichols, J. Terzic, B. I. Min, J. W. Brill, G. Cao, A. Seo, "Optical signatures of spin-orbit exciton in bandwidth controlled Sr_2IrO_4 epitaxial films via high-concentration Ca and Ba doping", Phys. Rev. B 95, 235125 (2017).

2. <u>J. H. Gruenewald</u>, J. Kim, H. S. Kim, J. M. Johnson, J. Hwang, M. Souri, J. Terzic, S. H. Chang, A. Said, J. W. Brill, G. Cao, H. Y. Kee, S. S. A. Seo, "Engineering

one-dimensional quantum-stripes from superlattices of two-dimensional layered materials", Adv. Mater. 29, 1603798 (2017).

3. S. S. A. Seo, J. Nichols, J. Hwang, J. Terzic, <u>J. H. Gruenewald</u>, M. Souri, J. Thompson, J. G. Connell, G. Cao, "Selective growth of epitaxial Sr_2IrO_4 by controlling plume dimensions in pulsed laser deposition", Appl. Phys. Lett. 109, 201901 (2016).

4. J. Thompson, J. Nichols, S. Lee, S. Ryee, <u>J. H. Gruenewald</u>, J. G. Connell, M. Souri, J. M. Johnson, J. Hwang, M. J. Han, H. N. Lee, D.-W. Kim, S. S. A. Seo, "Enhanced metallic properties of $SrRuO_3$ thin-film electrodes via kinetically controlled laser ablation", Appl. Phys. Lett. 109, 161902 (2016).

5. M. Souri, <u>J. H. Gruenewald</u>, J. Terzic, J. W. Brill, G. Cao, S. S. A. Seo, "Investigations of metastable Ca_2IrO_4 epitaxial thin-films: systematic comparison with Sr_2IrO_4 and Ba_2IrO_4", Sci. Rep. 6, 25967 (2016).

6. J. G. Connell, J. Nichols, <u>J. H. Gruenewald</u>, D.-W. Kim, S. S. A. Seo, "Conducting $LaAlO_3/SrTiO_3$ heterointerfaces on atomically flat substrates prepared by deionized-water", Sci. Rep. 6, 23621 (2016).

7. <u>J. H. Gruenewald</u>, J. Nichols, J. Terzic, G. Cao, J. W. Brill, S. S. A. Seo, *Invited Feature Paper:* "Compressive strain-induced metal-insulator transition in orthorhombic $SrIrO_3$ thin films", J. Mater. Res. 29, 2491 (2014).

8. <u>J. H. Gruenewald</u>, J. Nichols, S. S. A. Seo, "Pulsed laser deposition with simultaneous in situ real-time monitoring of optical spectroscopic ellipsometry and reflection high-energy electron diffraction", Rev. Sci. Instrum. 84, 043902 (2013).